Alma Mater Studiorum · Università di Bologna

Scuola di Scienze
Dipartimento di Fisica e Astronomia
Corso di Laurea in Fisica

Study of ion transport in organic electrochemical transistors (OECTs) for highly efficient bioelectronics interfaces

Relatore:
Prof. Beatrice Fraboni

Correlatore:
Filippo Bonafè

Presentata da:
Riccardo Maria Marabini

Anno Accademico 2022/2023

Sommario

La Bioelettronica studia l'integrazione fra dispositivi elettronici e sistemi biologici. Data la necessità di tradurre i segnali biologici in correnti elettriche, la Bioelettronica ha tratto grande beneficio dalla ricerca sui polimeri conduttivi come PEDOT:PSS. Questo materiale dimostra ottime qualità in termini di biocompatibilità, conducibilità, stabilità chimica e termica. I Transistor Elettrochimici Organici sono una delle applicazioni più promettenti del PEDOT:PSS. Sebbene gli OECT vengano impiegati con successo come sensori di impedenza grazie alle intrinseche proprietà di amplificazione, la dinamica del trasporto ionico che influenza la sensibilità del dispositivo richiede ulteriore ricerca. In questa tesi, abbiamo studiato come i potenziali applicati e la frequenza di funzionamento modifichino la distribuzione spaziale della corrente ionica nel canale semi-conduttivo. Abbiamo ottenuto una descrizione quantitativa del processo attraverso il calcolo sistematico della frazione di corrente che scorre verso il terminale di source, f_{OECT}.

Il dispositivo studiato è caratterizzato da una geometria di $W = 300\,\mu\text{m}$, $L = 100\,\mu\text{m}$, una mobilità di lacune di $\mu \approx (2.78 \pm 0.07)\,\text{cm}^2\,\text{V}^{-1}\,\text{s}^{-1}$ e una capacità volumetrica di $C^* = (36 \pm 4)\,\text{F}\,\text{cm}^{-3}$. Abbiamo studiato il dispositivo in un range di frequenze di $f = [10; 10^5]\,\text{Hz}$, trovando che $f_{OECT} \to \frac{1}{2}$ per $f > 10\,\text{kHz}$, dove il trasporto ionico è limitato alla corrente di spostamento all'interfaccia PEDOT:PSS-elettrolita. Alle basse frequenze, f_{OECT} è una funzione non banale dei potenziali DC di gate e di drain. In questo regime, la mobilità ionica nel PEDOT:PSS è abbastanza grande da permettere una distribuzione della carica lungo il canale, che altera lo stato di dragaggio del polimero e la conducibilità locale. Infine, abbiamo misurato i valori più grandi di f_{OECT} quando il source (o il drain) risultano completamente svuotati di cationi: condizione a cui corrispondono le correnti elettroniche maggiori.

Abstract

Bioelectronics studies the integration of electronic devices with biological systems. Given the necessity to transduce biological ionic signals into abiotic electric currents, Bioelctronics has benefited from the introduction of conductive polymers such as PEDOT:PSS. This material outperforms other conjugated polymers in terms of biocompatibility, conductivity, chemical and thermal stability. Organic Electrochemical Transistors are one of the most promising applications of PEDOT:PSS. OECTs have been successfully employed as impedance biosensors thanks to their intrinsic amplification properties, but the dynamics of ion transport affecting the device sensitivity still requires further insight. In this thesis, we investigated how the operating voltages and frequency alter the spatial distribution of the ionic current in the semiconducting channel. We achieve a quantitative description of the process by systematically calculating the fraction of current flowing towards the source electrode of the transistor, f_{OECT}.

The device is studied in a frequency range of $f = [10; 10^5]\,\mathrm{Hz}$ and is characterised by a geometry of $W = 300\,\mu\mathrm{m}$, $L = 100\,\mu\mathrm{m}$, a hole mobility of $\mu \approx (2.78 \pm 0.07)\,\mathrm{cm^2\,V^{-1}\,s^{-1}}$ and a volumetric capacitance of $C^* = (36 \pm 4)\,\mathrm{F\,cm^{-3}}$. For $f > 10\,\mathrm{kHz}$, we found that $f_{OECT} \to \frac{1}{2}$ for all combinations of DC potentials applied: ion transport is restricted to the ionic displacement current at the PEDOT:PSS-electrolyte interface. At low-frequencies, f_{OECT} is a not-trivial function of the gate and drain DC potentials. In this regime, ionic mobility in PEDOT:PSS is sufficiently large to allow for a non uniform distribution of charge along the channel, impacting on the doping state of the polymer and its local conductivity. Finally, larger f_{OECT} factors are measured when the source (or drain) electrode is depleted from cations, which entails a larger local doping level of PEDOT:PSS, resulting into higher electronic currents.

Contents

Chapter 1

Introduction

1.1 Bioelectronics

The field of Bioelectronics faces the intriguing challenge of interfacing electronic devices with living structures. Despite the resounding success gained in the past decades, this discipline dates back to the late 17^{th} century with the first pioneering experiments of Luigi Galvani on electric stimulation of muscles. Since then, Bioelectronics has grown and branched in order to comply with all the mechanisms which biological systems employ to carry information. The importance to detect and analyse such signals is manifest, indeed, over the past decade Bioelectronics has been gathering an increasing amount of attention thanks to its highly promising medical applications in both *in vitro* and *in vivo* analyses. Some of these will be revised in the following chapters such as electrodes, biosensors and drug delivery.
In the first place, biocompatibility, low toxicity, miniaturisation, specificity of the signals, chemical and mechanical durability are just some of the constraints posed by the targeted systems, which have a decisive impact on the materials employed to implement the devices. For this reason Bioelectronics has inconceivably benefited from the introduction of organic semiconducting polymers. These have actually paved the way for the rise of a novel branch named Organic Bioelectronics, a term coined by Magnus Berggren and Agneta Richter-Dahlfors in 2007 [1]. Organic materials meet with most of the requirements aforementioned, while adding some highly desirable features in terms of chemical modification and low-temperature processing [2]. Indeed some of these properties will be analysed in the following sections in relation to a widely studied conjugated polymer: poly(3,4-ethylenedioxythiophene) polystyrene sulfonate (PEDOT:PSS).

Organic Semiconductors

The first works on conjugated polymers date back to the '70*s* and were carried out by Nobel Prize laureates Alan J. Heeger, Alan G. MacDiarmid and Hideki Shirakawa.
A comprehensive definition of this class of materials reads as follows: conjugated polymers are organic macromolecules characterised by a backbone chain of alternating double- and single-bonds. The overlapping p-orbitals create a system of delocalised π-electrons, which can result in interesting and useful optical and electronic properties. The term conjugated refers to the conductive properties of these materials, as opposed to saturated polymers, which are insulating. Indeed, in saturated polymers all the electrons are employed in σ-bonds, hence, the conductive band is too far to be accessible. Conversely, in conjugated polymers there are spare π-electrons for each carbon atom which combine in a single structure exhibiting charge delocalisation along

the *back-bone*. A simple quantum model for the conductivity of a polymeric chain can be implemented easily. The macromolecule is modelled as a linear chain of N atoms equally spaced by a distance d, while π-electrons are completely delocalised along the chain. Therefore an electron can be treated as a free particle of mass m inside a one-dimensional potential box of lenght $L = d(N-1) \approx d * N$ (for $N \gg 1$). The time-independent Schroedinger equation for this system reads as

$$\frac{\hbar^2}{2m}\frac{\mathrm{d}\phi}{\mathrm{d}x} + w\phi = 0 \tag{1.1}$$

where $\hbar$ is the reduced Planck's constant, w is the energy eigenvalue and ϕ is a non identically vanishing spacial wave function which satisfies the following boundary conditions

$$\phi(0) = \phi(L) = 0 \tag{1.2}$$

The solution takes the simple form

$$\phi(x) = \left(\frac{2}{L}\right)^{\frac{1}{2}} \sin\left(\frac{\pi}{L}nx\right) \quad and \quad w_n = \frac{\hbar^2\pi^2}{2mL}n^2 \quad with \quad n = 1, 2, 3, ... \tag{1.3}$$

Assuming that each orbital is occupied by two electrons with opposite spins, the energies of the Highest Occupied Molecular Orbital (HOMO) and of the Lowest Unoccupied Molecular Orbital (LUMO) can be written as

$$E_{HOMO} = \frac{\hbar^2\pi^2}{2m}\frac{(N/2)^2}{(d*N)^2} \quad and \quad E_{LUMO} = \frac{\hbar^2\pi^2}{2m}\frac{(N/2+1)^2}{(d*N)^2} \tag{1.4}$$

The energy gap between these two levels is therefore

$$\Delta E_{gap} = E_{HOMO} - E_{LUMO} = \frac{\hbar^2\pi^2}{2md^2}\frac{N+1}{N^2} \approx \frac{\hbar^2\pi^2}{2md^2}\frac{1}{N} \quad for \quad N \gg 1 \tag{1.5}$$

From Eq. 1.5, an ideal infinite-long chain of equally spaced carbon atom behaves as a metal. However, since such structure is unstable, distortions arise to minimise energy to the expense of the symmetry of the system. This chemical conjugation results into a forbidden band gap and thus into semiconducting properties [3]. An example of the conjugated system of polyacetylene is depicted in Fig. 1.1, where carbon atoms are connected via alternating single and double bonds: the repeated unit of PA chains is [−CH=CH−] instead of [−CH−].
The low intrinsic conductivity of conjugated polymers can be enhanced with doping processes. The doping process of organic semiconductors is basically a redox reaction and, unlike the standard doping of inorganic semiconductors, it is usually a reversible process. In essence, for each polymeric cation (p-type) a reduced ion must be added, on the other hand for each polymeric anion (n-type) an oxidised ion is needed. To this end, there exist different types of doping: chemical, electrochemical, photochemical, acid-base reaction and charge injection [4].

- **Chemical doping** is basically a redox reaction between the polymeric chain and the dopant: oxidation produces a p-type doping, while reduction produces an n-type. Despite its simplicity, this procedure has poor results in terms of homogeneity of the doping.

- **Electrochemical doping** was developed to control the doping level more efficiently. This treatment employs an electrode to produce the charge for the redox of the polymer and it allows to set the doping level via the voltage applied to the electrode.

- **Acid-Base doping** offers an alternative way to translate the Fermi-level in the high density region of electronic states. In this case, the process consists of a protonation reaction, where the polymer turns from semiconducting into metallic state, as each monomer may carry a positive charge.

- **Photodoping** consists of promoting the production of an electron-hole couple via local absorption of a photon.

- **Charge injection** consists of injecting holes or electrons directly in the polymeric back-bone using metallic contacts. Unlike chemical methods, in this treatment there is no need for a counterion.

The first three methods induce permanent electrical conductivity, at least until all carriers are compensated or reverse doping is applied to the material. Conversely, in the latter two procedures carriers are available only as long as the perturbation is applied: photons or a voltage current respectively.

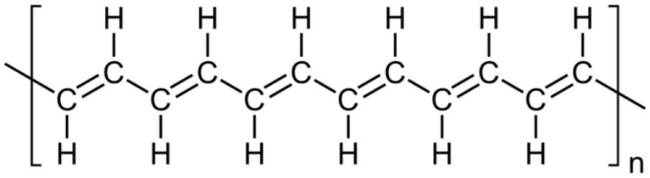

Figure 1.1: *Chemical structure of polyacetylene*

1.1.1 Organic Bioelectronics

A wealth of promising bioelectronic applications benefit form the development of organic materials. The comparison between Silicon and PEDOT:PSS is paradigmatic to understand the most relevant differences between inorganic and organic semiconductors, as depicted in Fig. 1.2 [2]. Indeed both can be p-type semiconductors: Silicon with Boron, while PEDOT with poly(styrene sulfonate) (PSS). However, in Silicon each atom is firmly held in place by four covalent bonds. On the other hand, the prevalence of van der Waals interactions among polymeric chains gives a more flexible structure to PEDOT:PSS. Hence, the strain mismatch between the device and the biological structure can be dramatically reduced. In addition, organic materials comply better with fabrication techniques which allow to tailor the geometry of the sensors according to the necessities of the system studied, boosting the adaptability of the device. Furthermore, from Fig. 1.2 it is manifest how the Silicon interface is oxidised, being littered with *dangling bonds*, while the polymer interface is *oxide-free* and has no broken covalent bonds, which not only allows it to be placed in direct contact with biological structures, but it also promotes cell adhesion. For example, it is possible to weave the polymer together with biological fibres [5] or even to deposit the organic layer directly on sensitive biological tissues without damaging them [6].
The large spacing between the molecules of the polymer allows for *efficient ion transport* through the interface even at room temperature, which gives rise to a volumetric capacity involving the whole semiconducting layer. Indeed, this is a prominent feature of organic semiconductors which can be exploited for designing highly efficient biosensors and bioactuators. For instance, organic devices outperform the inorganic equivalent when it comes to measuring small potential fluctuations [7]. Last but not least important, since ion diffusion involves the whole polymeric layer, doping and de-doping

processes alter the spacial structure of the chains, resulting in changes in the optical and mechanical properties: this finds immediate application in electrochromic displays [8], actuators for artificial muscles [9] and organic electronic ion pumps (OEIPs).
In addition, most organic materials allow for *facile chemical modification*: the modification of the π-conjugated backbone can be performed easily even at relatively low temperatures, and numerous additives may be employed to achieve unprecedented degrees of customisation. Finally, *transparency* is another feature which comes in handy in medical applications, as it allows visual assessment and optical imaging of the samples.

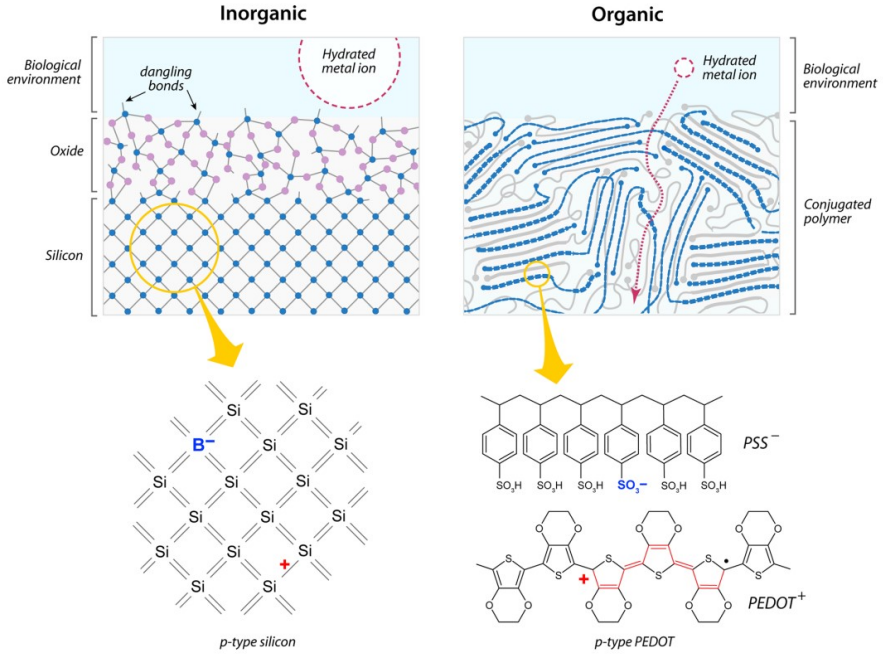

Figure 1.2: *Schematics of an inorganic semiconductor, Silicon, and an organic semiconductor, PEDOT, at the interface with an electrolyte. The hydrated ion is meant to be the same in both schematics, defining the relative lengths scale. The insets show the action of p-type dopants, Boron in Silicon, and PSS in PEDOT, respectively. [2]*

1.1.2 PEDOT

PEDOT is one of the most popular conjugated polymers thanks to its numerous desirable features. It was first synthesised by Bayer AG in 1989 as a derivative of polythiophene and its name stands for poly(3,4-ethylenedioxythiophene). Even though this monomer was selected for its high conductivity and long-term stability in the doped state, the properties of this material deserve a deeper analysis and they will be reviewed in the following paragraphs.

- **Reversible doping state**
  First and foremost, PEDOT benefits form reversible doping without showing significant drawbacks. The doping state has a chromatic effect on the polymer which changes from light to dark blue as the doping state turns from p-type to n-type: this property can be exploited in electrochromic displays.

- **Chemical and Thermal stability**
  PEDOT can withstand relatively high temperatures: its degradation starts at around 150 °C and is complete at 390 °C. In addition, its conductive properties

show great stability over time. Last but not least, PEDOT has a low redox voltage compared to other equivalent polymers.

- **Regularity of the structure**
  PEDOT's chains are shorter than thiophene ones. This promotes the three-dimensional regularity while suppressing the probability of defects in the structure.

- **Small *band gap***
  The intrinsic energy gap settles around 1.5 eV, (compatible with the one of GaAs), and it runs lower than 1 eV in the doped state. Hence, conductivity up to $0.5\,\mathrm{kS\,cm^{-1}}$ can be achieved.

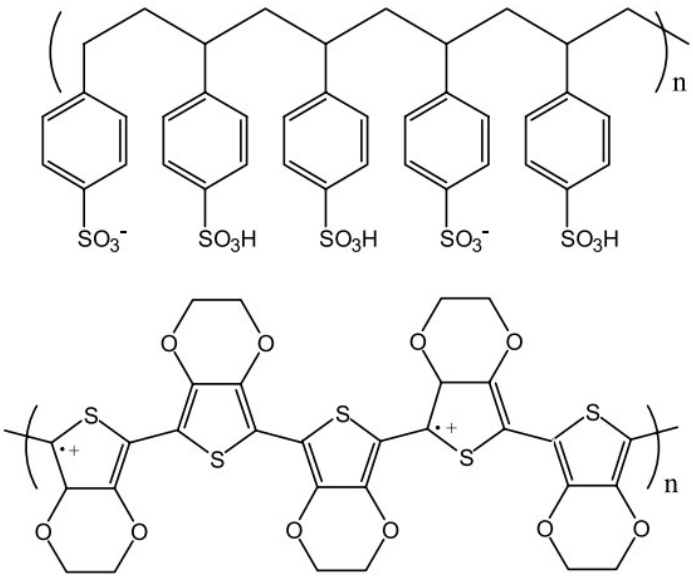

Figure 1.3: *Chemical structure of poly(3,4-ethylenedioxythiophene) polystyrene sulfonate (PEDOT:PSS)*

PEDOT:PSS

PEDOT is usually coupled with the polyanion poly(styrene sulfonate) (PSS) to form a complex polyelectrolyte as shown in Fig. 1.2 and more in detail in Fig. 1.3. PSS counterbalances the positive charge of PEDOT ions. Besides, it allows the formation of a stable micro-dispersion of insoluble PEDOT in water, which enhances film-forming properties. This material shows high conductivity, σ, up to $1\,\mathrm{kS\,cm^{-1}}$, comparable to metallic ones. In particular, conductivity is due to holes in PEDOT oxidised units only, while PSS has mainly a structural function. Charge transport can be thought as a *hopping* process of holes akin to the one of amorphous organic semiconductors: an hypothesis which supports the observed dependence of conductivity on temperature as well. As for any semiconducting material, conductivity, σ, is given by the expression:

$$\sigma = e[\mu_p n_p + \mu_n n_n] \tag{1.6}$$

where e is the elementary charge, μ_p, n_p are holes mobility and density respectively, μ_n, n_n are mobility and density of electrons. However, since in PEDOT:PSS any free

electron immediately recombines with the positive tyophene ions, mobility of holes only may be taken into account. Thus, PEDOT:PSS is a p-type semiconductor and its high doping states are characterised by a hole density of $n_p \approx 3 \times 10^{20}\,\mathrm{cm}^{-3}$ and conductivity of $\sigma_p \approx 1\,\mathrm{kS\,cm}^{-1}$, which results into a hole mobility of $\mu_p \approx 5\,\mathrm{cm}^2\,\mathrm{V}^{-1}\,\mathrm{s}^{-1}$.

1.1.3 PEDOT:PSS thin film deposition

PEDOT is hydrophobic and, thus, it must be coupled with poly(styrene sulfonate) (PSS) to obtain a micro-dispersion in water, which is extremely advantageous when it comes to produce thin films. This solution brings about two more significant benefits: on the economic side, PEDOT:PSS can be easily commercialised on industrial scales, reducing the costs of production, on the physical one, transparency allows to performe optical measurements easily.
The *film-forming* properties of PEDOT:PSS can be altered almost to taste by varying PEDOT and PSS relative concentrations and by adding stabilisers and surfactants, which improve wettability.
There exist two main categories of deposition for PEDOT:PSS: *coating* and *printing*. The main difference is that in the former, the polymer covers the entirety of the surface available, while in the latter the *ink* is transferred to preset sites only. In addition, electrodeposition must be mentioned, for this technique has proved extremely successful in depositing PEDOT networks directly on living structures [10]. Examples of *printing* procedures include screen printing, flexographic printing, pad printing, ink-jet printing and nozzle printing. On the other hand, *Coating* techniques include spin coating, spray coating, painting, slit coating and bar coating. Spin coating will be analysed in greater detail since the devices covered in this work were produced with such method.

Spin coating

The idea behind spin coating is straightforward. First, a quantity of the polymer is deposited on the sample to process, which is made rotate at a constant angular velocity ω until the material forms a uniform film (pictorial representation in Fig. 1.4). Geometric properties of this film depend on ω and the chemical properties of the polymer: viscosity, volatility, specific weight and mass of the molecules. The experimental relation between the thickness of the layer, d, and such parameters is $d = k\omega^{\alpha}$, where k depends on viscosity and $\alpha \approx -0.5$. Despite the significant loss of material, this process shows high standards of reproducibility of thin layers over small areas of $\sim \mathrm{cm}^2$.

1.1.4 Some Applications

Applications of organic polymers come in a wide variety of fashions thanks to the numerous properties revised in Sec. 1.1.1. At the very beginning, organic materials played a slightly marginal role since they were used especially as passive coatings to improve biocompatibility of metallic probes. However, a radical improvement was achieved when organic semiconductors turned from passive into active components. From then on, a wealth of organic-based devices has been successfully developed and, in the following section, some of the most noteworthy ones for *in vitro* and *in vivo* analysis will be reviewed.

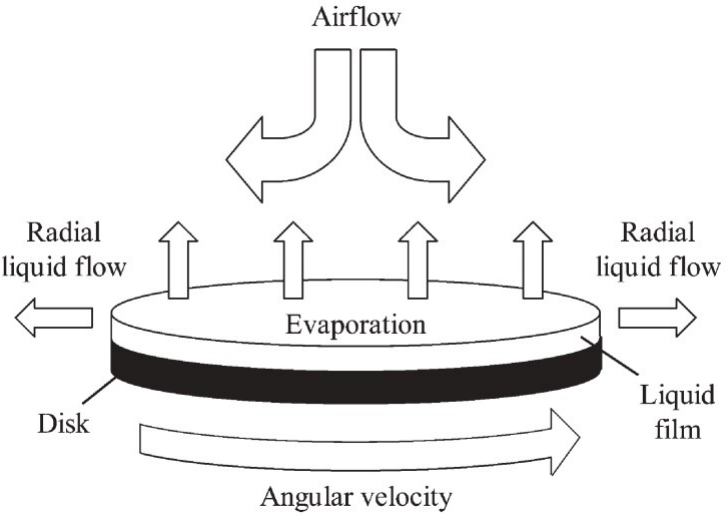

Figure 1.4: *Schematic of the spin-coating process [11]*

Electrodes

Electrodes are among the most straightforward applications. An electrode consists of a conductive probe (metallic or organic) which can be placed in direct contact or in the nearby of the area of interest. The traditional materials employed are metals such as Platinum (Pt) and Tungsten (W). However, inorganic electrodes have numerous drawbacks in terms of compatibility with the biological milieu as they have fixed characteristics which hamper the adaptation of the sensor to the surrounding environment. Monitoring of neural activity is one of the typical applications of electrodes, still, it has been observed that an inflammatory response usually follows the implantation of the device, which can result in poor integration with the target and shielding of the signal due to the thickening of the tissue. In order to tackle this problem, organic semiconductors (e.g. polypyrrole (PPy)) have been employed to coat metallic wires [12]: the coating resulted in a decrease in chemical reactions at the interface and a larger capacity if compared to bare wires. In addition, this adjustment allowed to increase the surface of the sensor as well, improving the transduction of the signal.
However, as biological structures do not usually form planar structures, the great leap forward was made through the development of three dimensional structures composed of organic semiconductors only [13], onto which cells can grow freely and signals can propagate with the least perturbation.
Furthermore, the growth of neurons can be electrically stimulated, opening a wide range of possibilities for neural recovery devices. Finally, it has been proved that layers of organic semiconductors can be deposited directly onto living structures [6] [10]. This technique, if engineered, could bring the quality of the interface at an upper level: not only could invasive operations be avoided, but the polymer would also interweave with the cells, boosting the surface contact of the sensor.

Biosensors

Biosensors are devices that exploit biochemical reactions to detect chemical compounds. Indeed, they can be formally visualised as two-step systems: first comes the recognition of the chemical compound then the transduction of the response into a detectable signal. The former can be made of any biological transducer such as enzymes, tissues, organelles or even entire cells, and the rub lies in coupling those systems with the

electronic transducer.
The chief examples of biosensors are Organic Field Effect Transistors (OFETs) and Organic Electrochemical Transistors (OECTs). These devices usually employ macromolecules (DNA, enzymes, proteins or antibodies) to turn biological signals into an event that affects conductivity of the organic semiconductor of the transistor. Along with their miniaturisation potential, these devices can be made fully flexible thanks to advances in conducting, semiconducting and insulating inks [14].
Glucose sensors are a noteworthy application of the double-step mechanism. These sensors rely on the redox reaction performed by glucose oxidise enzyme (GOx), and the subsequent collection of electrons by an electrode. Another application sees OECTs employed as impedance sensors to assess cell layers integrity. This procedure has been successfully tested in researching the response of neutralising antibodies towards different viruses [15] [16], and it has proved to be a time-saving solution thanks to its fast and real-time monitoring, if compared to optical analyses.
Finally, the growth of cell layers and tissues is by now a standard procedure of molecular biology which can be partly automated via organic bioelectronics, with the bonus of controlling the thickness of the layers as well. Indeed, it has been found that cell growth can be either fostered or suppressed according to the redox state of the polymer onto which they are deposited [17]. This effect was exploited to create a channel of Indium (In) coated with PEDOT:Tos, where a potential applied to its ends produces a gradient of the redox state of PEDOT, yielding a cell culture of varying thickness [18].

Drug delivery

Drug may consist of any type of molecules, ranging form simple ions to large and bulky molecules, however the efficacy of a treatment highly depends on the rate at which it is delivered. Conventional endovenous methods compromise between toxicity and the effective duration of the therapy, hence, the challenge is to produce devices that supply the drug only when needed and with the correct concentration.
Initially, the very first idea was to mingle the organic semiconductor with the specific drug, and to control the release of the latter via reversible redox reactions. However, this has required a fine work of specialisation of the polymers in order to increase the amount of drug carried and to control the off- and on-switching of the device efficiently.
A more recent and sophisticated solution is offered by Organic Electronic Ion Pumps (OEIPs) [19], where the voltage applied controls the flux of ions from a reservoir to a target, connected via an organic channel which allows ionic currents but not electronics ones: for PEDOT:PSS this state can be achieved by over-oxidising PEDOT.

1.2 OECTs

Transistors are some of the most widespread electronic component nowadays. Their history dates back to 1947 and despite many further developments, transistors' physics is pretty unchanged. Basically, a transistor consists of a semiconducting material wired to the external world by three electrodes.
Transistors are usually employed for their amplification properties and the application of such technology for sensing usually requires a high gain factor and high transconductance. However, biological systems pose numerous further restrictions in terms of biocompatibility and mechanical flexibility. If traditional inorganic semiconductors performed well in the first two categories, this does not happen for the latter two. This gave rise to the interest towards organic semiconducting polymers as efficient substi-

tutes, and after the initial research, this class of materials has known a period of growth and prosperity.
Some noteworthy applications have been revised in Sec. 1.1.4 of this chapter and the present work will focus on one of the most promising: organic electrochemical transistors (OECTs). OECTs belong to a much wider class of electrolyte gated transistors (EGTs), where the gate is connected to the other two terminals via an electrolyte, which makes these devices compatible with aqueous milieus. An OECTs is a peculiar configuration of EGTs where the semiconducting material is in direct contact with the electrolyte, allowing the transport of ions through the bulk of the semiconductor. The first OECT was produced in 1984 by Wrighton *et al.* [20] using polypyrrole, and from then on a wide range of polymers has been employed, among which PEDOT:PSS stands out.

1.2.1 Structure

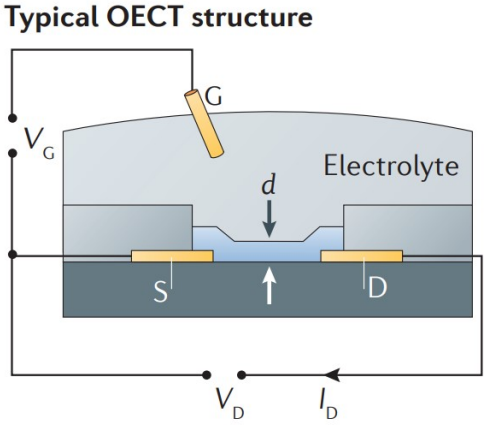

Figure 1.5: *The typical structure of an organic electrochemical transistor (OECT), showing the source (S), drain (D), electrolyte and gate (G). d is the thickness of the organic film [21]*

OECTs are three-terminal devices and, as displayed in Fig. 1.5, their structure consists of a channel, three terminals, source (S), drain (D) and gate (G), and an electrolyte, which comes as liquid, solid or gel. The channel is usually made of a semiconducting material deposited as a thin film onto a substrate (e.g. glass or plastic), while the gate is usually placed inside the electrolyte. Given that the source terminal is usually grounded, the operational parameters of an OECT are the voltage applied to the drain, V_{DS}, and the voltage applied to the gate, V_{GS}. The former results into a current between source and drain, I_D, while the latter acts as modulation of such current. Indeed, the distinctive trait of an OECT is the permeability of the polymeric channel to ions of the electrolyte: the voltage applied to the gate is a handle for modulating the doping state of the semiconductor by reversibly injecting or extracting ions, and thus piloting the conductivity of the channel. This is the logic underlying the application of OECTs as potentiometric or impedance sensors: the biological signal comes as a little perturbation of the environment of the electrolyte, which however impacts a much larger current, I_D, in a detectable way.
OECTs are implemented in depletion mode, which means that the application of a gate voltage, V_G, de-dopes the semiconductor. In particlular Fig. 1.6 offers a good pictorial representation of the functioning of a PEDOT:PSS-based OECT when a voltage is applied to the gate, V_G. Qualitatively, when a positive voltage is applied to the gate,

$V_G > 0$, cations are injected into the bulk of the polymer and conductivity decreases. Conversely, if the gate voltage decreases, conductivity increases. However, what makes PEDOT:PSS an efficient transducer of biological signals is the reversibility of this process, as described by the following reaction [22]:

$$\text{PEDOT}^+\text{:PSS}^- + \text{M}^+ + \text{e}^- \rightleftharpoons \text{PEDOT} + \text{PSS}^-\text{M}^+ \tag{1.7}$$

where M^+ is a generic cation and e^- is an electron deriving from the source terminal. De-doping is the result of the de-coupling of the two polymers: despite the positive voltage of the gate, PSS^- is too massive to migrate out the polymeric matrix, and combines with the cations injected from the electrolyte. In order to maintain overall neutrality, an electron is extracted from the source and it reduces a PEDOT monomer, which turns neutral and insulating. When the gate voltage is removed, cations diffuse back in the electrolyte and PEDOT resumes its oxidised conductive state again. The major upside of this process is that conductivity may vary through several orders of magnitude just upon the application of a gate voltage of few volts.

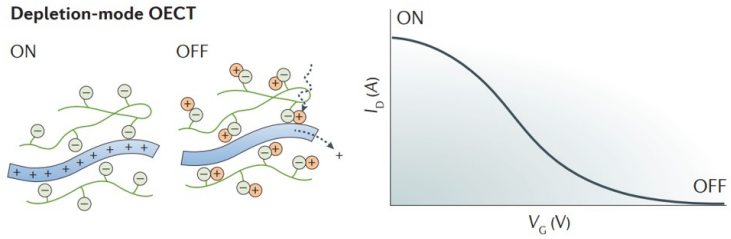

Figure 1.6: *Transfer curve showing depletion-mode operation of an OECT with a p-type conducting polymer channel. At zero gate voltage, holes on the conducting polymer contribute to a high drain current and the transistor is ON. When a gate voltage (positive) is applied, the holes are replaced by cations and the transistor is OFF [21]*

1.2.2 Device Physics

As traditional transistors, OECTs transduce small voltage signals applied to the gate into large changes in the drain current. The plot showing the dependence of the drain current from the gate voltage is called transfer curve, an example is reported in Fig. 1.6. Transconductance, g_m, is defined by the following equation and it is connected to the sensitivity of the device.

$$g_m = \frac{\partial I_D}{\partial V_G} \tag{1.8}$$

Therefore, transconductance is the chief merit parameter of the efficacy of an OECT. Usually OECTs attain large transconductance values thanks to the interaction of ions with the almost entirety of the channel.

One of the most popular models used to describe the working principle of a OECT is Bernards and Malliaras' model [23]. In order to understand the behaviour of the device, the OECT is split into an electronic and a ionic circuit as shown in Fig. 1.7. This model yields good results for the explanation of the steady-state and the transient response, which will be reviewed in the following sections. From now on, nomenclature will refer to p-type semiconducting channel, although the same considerations can be swiftly applied to n-type semiconductors.

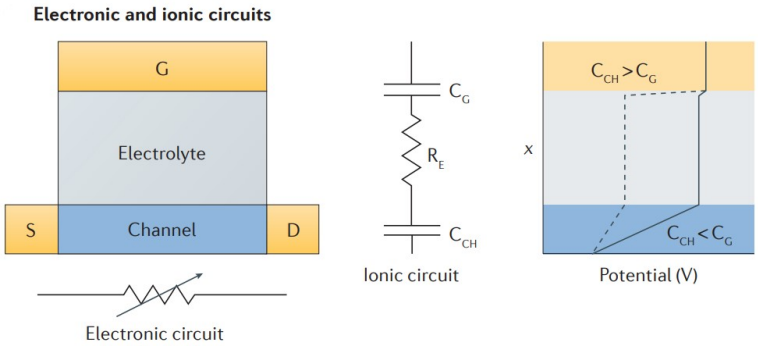

Figure 1.7: *Ionic and electronic circuits used to model OECTs. The electronic circuit, shown below the device layout on the left, is modelled as a resistor with a resistance that varies upon gating. The ionic circuit, shown in the middle, consists of capacitors corresponding to the channel, C_{CH}, and gate, C_G, respectively, and a resistor corresponding to the electrolyte, R_E. The panel on the right shows the distribution of potential in the ionic circuit. The solid line corresponds to the case of efficient gating, in which most of the applied gate voltage drops at the electrolyte–channel interface, driving ions inside the channel. The dashed line corresponds to the case of poor gating, where most of the applied gate voltage drops at the gate–electrolyte interface. [21]*

Electronic circuit

The electronic circuit consists of a p-type organic semiconductor film that transports holes between source and drain electrodes. Therefore it can be modelled plainly as a variable resistor (left panel of Fig. 1.7): thus, it is simply described by Ohm's law. In much the same way as MOSFETs, the microscopic formulation can be written as

$$J(x) = e\mu p(x)\frac{\mathrm{d}V(x)}{\mathrm{d}x} \tag{1.9}$$

where J is the current flux, e is the elementary charge, μ is the hole mobility, p is the hole density and dV/dx is the electric field. Mobility is assumed to be constant, otherwise no analytical solution would be available.
As described more in detail in the previous section, when a positive voltage is applied to the gate, $V_G > 0$, the concentration of holes decreases. The de-doping reaction described by Eq. 1.7 shows that this is a one-to-one process, from which the following linear relation is deduced:

$$p = p_0\left(1 - \frac{Q}{ep_0\mathcal{V}}\right) \tag{1.10}$$

where p_0 is the initial hole density in the organic semiconductor before the application of a gate voltage, Q is the total charge of the cations injected in the organic film from the electrolyte and $\mathcal{V}$ is the total volume of the semiconductor. All densities are considered to be uniform through the thickness of the semiconductor, which confines the validity of the model to thin films only.

Ionic Circuit

The middle panel of Fig. 1.7 depicts the ionic circuit: basically it consists of a resistor, R_E, modelling the ionic flow in the electrolyte, in series with a capacitor, C_d, which accounts for storage of charge at the organic film-electrolyte and gate electrode-electrolyte polarisable interfaces. Namely, C_d is the series of the the gate capacitor C_G and the channel one, C_{CH}. In Bernards model interfaces are governed by purely capacitive

processes, which implies that ions injected into the channel compensate the presence of opposite charges electrostatically, without starting faradaic processes. When a positive voltage is applied to the gate, V_G, the transient response of the charge in the capacitor is the same as a RC series circuit:

$$Q(t) = Q_{ss}[1 - \exp\{-t/\tau_i\}] \tag{1.11}$$

where $Q_{ss} = C_d \Delta V$ is the total charge that flows in the transient (ΔV is the potential applied through the electrolyte) and $\tau_i = R_E C_d$ is the ionic transient time. For convenience, let us define $c_d = C_d/A$ as the capacitance per unit area, where A is the area of the device studied. For the sake of simplicity, c_d is assumed to be independent from the voltage applied.
The diagram on the right of Fig. 1.7 shows an important phenomenon, related to the efficiency of the gate: the solid line is associated to good gating conditions (potential applied shows a significant drop across the channel), while the dashed one describes poor gating, where the larger potential drop occurs at the gate-electrolyte interface. In the model, C_G is in series with the channel one, C_{CH}, as a consequence the larger potential drop occurs through the smaller capacitor. Therefore, good gating occurs if $V_G \gg V_{CH}$, unfortunately meeting with this condition is no easy task, because of the large volumetric capacitance of the semiconducting polymer. This issue can be overcome either by increasing the surface of the gate or by using a non-polarisable gate electrode, such as AG/AgCl, through which the potential drop is negligible [21].

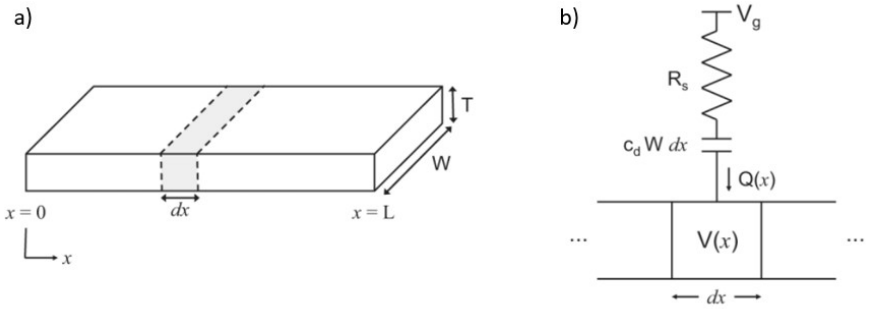

Figure 1.8: *Geometric reference of the model:* ***a)*** *geometry of the channel: L is the length, W the width and T the thickness.* ***b)*** *detail of the ionic circuit in a specific location of the channel, x.*
The origin of the system is placed at the source terminal, while the drain is at x = L. [23]

1.2.3 Stationary behaviour

In the stationary condition, ionic current tends asymptotically to zero and C_d is fully charged. In order to find the behaviour of the current in the channel, the spatial distribution of holes, p, must be known, and thus Q. In fact, the ionic charge injected in the polymer is actually a function of the position along the channel, $Q := Q(x)$, which from Eq. 1.11 reads as

$$for \quad t \to \infty, \quad Q(x,t) \to Q_{ss}(x) = c_d W\Big(V_G - V(x)\Big)dx \tag{1.12}$$

where V_G is the gate voltage, $V(x)$ is the spatial voltage profile along the organic film, W is the widht and dx the infinitesimal length of the organic film. Combining this

result with Eq.s 1.9-1.10, the current flowing in the channel at steady state in an OECT is

$$J(x) = e\mu p_0 \left[1 - \frac{V_G - V(x)}{V_t}\right] \frac{\mathrm{d}V(x)}{\mathrm{d}x} \tag{1.13}$$

where V_t is the threshold voltage, defined as $V_t = ep_0T/c_d$, where T is the thickness of the film. This equation can be solved imposing that the source-drain current density is spatially constant. In the first quadrant, $V_D > 0$, two different regimes can be denoted:

$$I_D = G\left[1 - \frac{V_G - 1/2V_D}{V_t}\right]V_D \quad for \quad V_D < V_G \tag{1.14a}$$

$$I_D = G\left[V_D - \frac{V_G^2}{2V_t}\right] \quad for \quad V_D > V_G \tag{1.14b}$$

where G is the conductance of the organic semiconductor film, $G = e\mu p_0 WT/L$. In the first regime, $V_D > 0 \wedge V_D < V_G$, de-doping occurs uniformly along the whole channel, while for $V_D > 0 \wedge V_D > V_G$, de-doping will only occur where $V(x) < V_G$. Notably, in this latter region, I_D exhibits a linear dependence on V_D.
In the third quadrant, $V_D \leq 0$, de-doping occurs anywhere along the channel as soon as positive gate voltage is applied. Namely, it is possible to deplete entire regions where ion concentration equals intrinsic hole density, p_0. This condition can be expressed as $V_G - V_D \geq V_t$, defining the critical saturation drain voltage as $V_D^{sat} = V_G - V_t$. However, in the same fashion as Field Effect Transistor, the holes injected in the neutral region are still attracted by the drain. Further considerations must be made upon the impact of the length of the channel on the drain current. For short-channelled devices, as $|V_D|$ increases, the depletion region can have a significant extension, and I_D will keep on soaring as well. On the other hand, in the limit of long channels, the depletion region will not affect the source in a relevant way, and for $|V_D| \geq |V_D^{sat}|$ the current in the saturation regime is

$$I_D = -\frac{G\left(V_D^{sat}\right)^2}{2V_t} \tag{1.15}$$

These regimes are summarised in Fig. 1.9, where the output curves of an OECT for different combinations of V_D and V_G are plotted.

This model can predict the dependence of transconductance on the geometric characteristics of the device and on the experimental parameters [24]. In the linear regime, derivation of Eq. 1.14a leads to

$$g_m^{lin} = -\mu C^* \frac{WT}{L} V_D \tag{1.16}$$

where C^* is the volumetric capacity, while in the saturation regime, g_m^{sat} is given by derivation of Eq. 1.15 and it reads as

$$g_m^{sat} = \mu C^* \frac{WT}{L} \left[V_G - V_t\right] \tag{1.17}$$

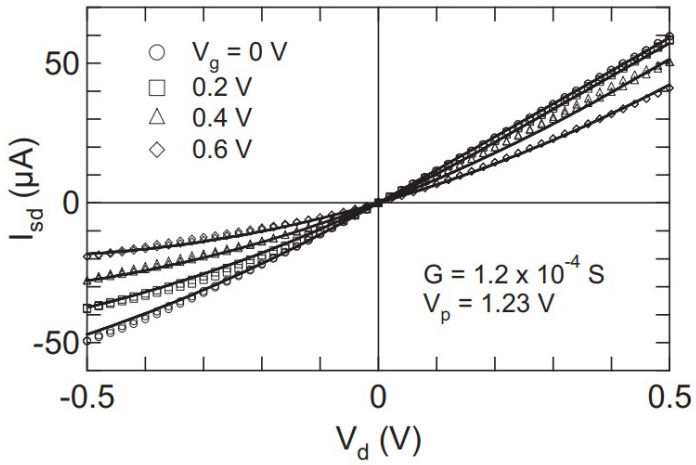

Figure 1.9: *Experimental steady-state current–voltage characteristics (data points) for an OECT fitted to modelled stead-state current–voltage characteristics (solid lines).[23]*

1.2.4 Transient response

The transient behaviour of the whole device can be analysed as the result of the transient responses of the two circuits analysed above. Therefore, two dominant effects ought to be considered: the injection of a cation from the electrolyte into the organic film and the removal of a hole at the source electrode. Neglecting the dependence on space of the voltage along the channel and of the holes concentration, the total current flux reads as

$$J(t) \approx e\mu p(t)\frac{V_D}{L} + eLf_{OECT}\frac{\mathrm{d}p(t)}{\mathrm{d}t} \tag{1.18}$$

where f_{OECT} is a proportionality constant accounting for the spatial non-uniformity of the de-doping process, which includes much of the complexity of the transient response. f_{OECT} describes the fraction of ionic current that contributes to source current. Substituting p with Eq. 1.10, the current along the channel reads

$$I(t) \approx G\left(1 - \frac{Q(t)}{ep_0\mathcal{V}}\right)V_D - f_{OECT}\frac{\mathrm{d}Q(t)}{\mathrm{d}t} \tag{1.19}$$

where $Q(t)$ is the transient response of the ionic circuit described above. To study $Q(t)$, two experimental conditions can be imposed: both the gate current, I_G, and the gate voltage, V_G, are constant during the transient. The first condition results into a linear dependence of the drain current on time:

$$I(t; I_G) = I_0 - I_G\left(f_{OECT} + \frac{t}{\tau_e}\right) \tag{1.20}$$

where $\tau_e = \frac{L^2}{\mu V_D}$ is the electronic transient time.
The second condition needs further considerations. Keeping V_G constant allows to employ Eq. 1.11, yet, it is necessary to assume that de-doping occurs uniformly along the channel without saturation effects. In order to ensure compatibility with the steady state current, an average potential difference of $\Delta V = V_G - 1/2V_D$ is used to obtain the transient response of OECT, which is described by equation

$$I(t; V_G) = I_{ss}(V_G) + \Delta I_{ss}\left(1 - f_{OECT}\frac{\tau_e}{\tau_i}\right)\exp\{-t/\tau_i\} \tag{1.21}$$

where $I_{ss}(V_G)$ is the stationary drain current at gate voltage V_G, while $\Delta I_{ss} = (I_{ss}(y)]_{V_G}^0$. Fig. 1.10 a) depicts the two possible responses: for $\tau_i \geq f_{OECT} * \tau_e$ the profile follows a monotonic decay, whereas for $\tau_i \leq f_{OECT} * \tau_e$ a spike-recovery trend is witnessed. Qualitatively, the former can be associated to a fast electronic response, while the latter may be due to poor hole transport and shows that the transient response is dominated by hole extraction from the film. The response of the device is determined basically by the ionic and electronic time responses: τ_i and τ_e respectively. Using Gouy–Chapman theory for double layer capacity the dependence of τ_i on constructive parameters is $\tau_i \sim \ell/C^{\frac{1}{2}}$: where ℓ is the distance of the electrode from the channel and C is the ionic concentration of the electrolyte. Hence, the ratio $\tau_e/\tau_i \sim \ell L^2/(\mu V_D)$ shows that the response can be tuned acting on the electrode location, the organic film length or the drain voltage, Fig. 1.10 b).

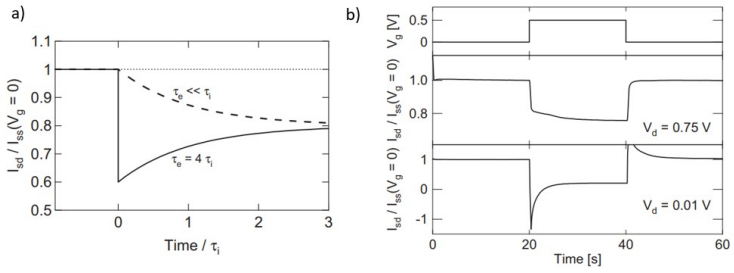

Figure 1.10: ***a)*** *Modelled source-drain current transient for a constant drain voltage. The two regimes of τ_e/τ_i are clearly visible: the dashed line represents the condition $\tau_i \geq f_{OECT} * \tau_e$, while the solid one shows the peak-recovery response associated to $\tau_i \leq f_{OECT} * \tau_e$.* ***b)*** *Experimental evaluation of the dependence of source-drain current transient for different values of the drain voltage. Source-drain current is normalised to the source-drain current prior to applied gate voltage, $I_{ss}(V_G = 0)$.*
τ_e and τ_i are the electronic and ionic time constants respectively, f_{OECT} is a proportionality constant accounting for the spatial non-uniformity of the de-doping process. [23]

1.2.5 AC amplification properties

OECTs are employed mainly as chemical biosensors, biosignal recording sensors and impedance biosensors. In particular, this last application offers numerous advantages when monitoring cellular adhesion and cell layer barrier properties. Investigating the changes of cell adhesion is of utmost importance as it may be a distinctive trait of a range of diseases including arthritis, cancer, osteoporosis and atherosclerosis [25] [26] [27] [28]. OECT-based impedance sensing offers a non-invasive and cost effective solution with respect to other techniques involving expensive equipment, which may interfere with the physiology of the structures [29]. Impedance sensing is performed in AC voltage conditions, however, despite the promising results, the thorough comprehension of the dependence of the transistor amplification gain on frequency has not been achieved yet.
To this end, Bernard's model logic can be adjusted according to the requirements of the circuital scheme displayed in Fig. 1.11. Even in AC conditions, we can model the OECT with an electronic and a ionic circuit. The electronic current in the channel is driven by a DC voltage applied to the drain, $V_{D,DC}$. The ionic circuit is still composed of a resistance, Z_{el}, and a capacitor, C_{ch}, which models ionic charge accumulation in the polymeric bulk. In AC measurements a frequency modulation, $V_{G,AC}$, is applied to

the DC potential of the gate electrode, $V_{G,DC}$. This gives rise to an AC ionic gate current which contributes to the current in the polymeric channel. Any object interposed between the gate and the channel alters the ionic flow by modifying the impedance of the ionic circuit, and ultimately the current at the source electrode. The total AC current at the source electrode is the combination of these two contributions and it can be written as follows:

$$I_{S,AC} = I_{ch,AC} + f_{OECT} I_{G,AC} \tag{1.22}$$

where $I_{ch,AC}$ is the AC current of the channel, $I_{G,AC}$ is the AC ionic current and f_{OECT} has been introduced in Eq. 1.18. The symbolic analysis of the circuit allows to express $I_{G,AC}$ as

$$I_{G,AC} = \frac{V_{G,AC}}{Z_G}, \quad with \quad Z_G = Z_{el} + Z_{ch} = Z_{el} + \frac{1}{i\omega C_{ch}} \tag{1.23}$$

where Z_G is the equivalent impedance of RC series and i is the imaginary unit. $I_{G,AC}$ is the current that corresponds to the micro-electrode configuration. A micro-electrode is a passive device which does not exhibits amplification properties since no potential is applied to the channel, $V_D = 0$. Following the definition of transconductance, the AC current in the channel takes the simple form

$$I_{ch,AC} = g_m V^*_{G,AC} \tag{1.24}$$

where $V^*_{G,AC} = V_{G,AC} - I_{G,AC} * Z_{el}$ is the actual gate potential applied to the channel after the potential drop through impedance Z_{el}.
The chief merit parameter of impedance sensors is sensitivity. For an OECT, sensitivity can be defined as $S_{OECT} = \frac{\partial I_{S,AC}}{\partial Z_G}$, which is the ability to transduce any variation of Z_{el} in a detectable output current. Substituting Eq. 1.22 in the definition and assuming that f_{OECT} is independent of Z_{el}, S_{OECT} is the sum of two contributions:

$$S_{OECT} = \left| \frac{\partial I_{ch,AC}}{\partial Z_{el}} + f_{OECT} * \frac{\partial I_{G,AC}}{\partial Z_{el}} \right| = |S_{ch} + f_{OECT} * S_{\mu E}| \tag{1.25}$$

where the explicit expressions of the channel sensitivity S_{ch}, and of the micro-electrode sensitivity $S_{\mu E}$ read as follows:

$$S_{ch} = \frac{g_m}{Z_G}\left(1 - \frac{Z_{el}}{Z_G}\right) V_{G,AC} = g_m V_{G,AC} \frac{i\omega C_{ch}}{1 + i\omega C_{ch} Z_{el}} \tag{1.26a}$$

$$S_{\mu E} = \frac{1}{Z_G^2} V_{G,AC} = \frac{V_{G,AC}}{\left(Z_{el} + \frac{1}{i\omega C_{ch}}\right)^2} \tag{1.26b}$$

Understanding how S_{OECT} depends on the geometry and the working point of the device is mandatory in order to produce highly efficient sensors. From the previous equations it is apparent how the channel and the micro-electrode sensitivities vary according to configurational parameters. However, the same cannot be said for f_{OECT}. Indeed, despite its importance, the characterisation of f_{OECT} still poses different challenges, and the aim of this work is to study how the segregation of the ionic current is affected by different bias potentials. Namely, since f_{OECT} is related to the dynamics of ion transport in the PEDOT:PSS channel, our study may lead to further understanding of this process in organic semiconductors.

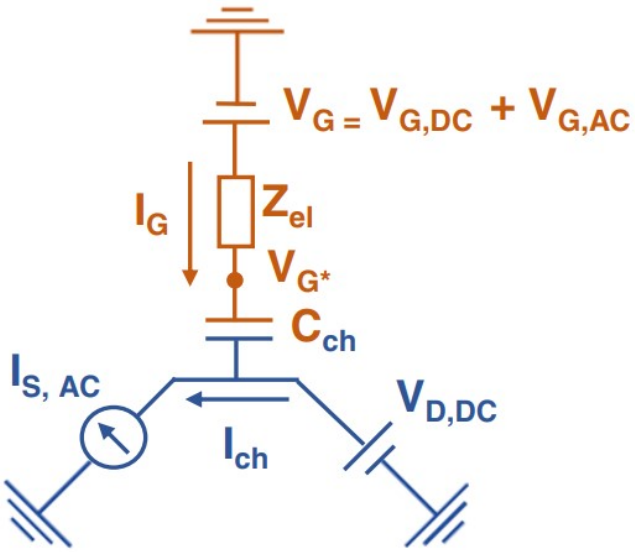

Figure 1.11: *Circuital model of an OECT in AC conditions: in orange the ionic circuit, in blue the electronic one.* $V_G = V_{G,DC} + V_{G,AC}$ *is the voltage applied to the gate,* $V_{D,DC}$ *the one applied to the drain.* V_G^* *is the actual gate potential applied to the channel, because of the drop caused by impedance of the electrolyte* Z_{el}*.* C_{ch} *is the capacitance of the channel. [30]*

Chapter 2

Materials and Methods

2.1 Microfabrication of an OECT

In this section the procedure for the fabrication of a PEDOT:PSS-based OECT is reviewed thoroughly. The configuration implemented is shown in Fig. 2.3. Each sample hosts nine devices, with five different geometries of the channel, and it is realised onto a glass slide, $50 \times 25\,\mathrm{mm}^2$. The microfabrication protocol involves three steps: micropatterning of metal electrodes, encapsulation and micropatterning of PEDOT:PSS.

Figure 2.1: ***a)*** *picture of the evaporation chamber* ***b)*** *MicroWriter ML 3 employed for laser lithography (Durham Magneto Optics)* ***c)*** *Spin coating set-up under extraction hood: on the left there is the hot plate, while on the right there is the spin coater.*

Micropatterning of metal electrodes

We patterned metal electrodes by means of subsequent evaporation of Chromium, Cr and Gold, Au, both 99.9% pure. Each electrode is composed by a contact, a pad to connect the contact to the external electronics and a feed-line connecting the pad with the contact. The Chromium layer promotes the adhesion of gold. The choice of gold is

driven by multiple factors: it creates ohmic contacts with the semiconducting polymer (PEDOT:PSS namely), it does not induce Faradaic processes in the potentials applied and it has a low level of oxidation.
First, we cleaned the glass substrate by sonication in water and soap (10%)/acetone/isopropanol/distilled water baths. After a dehydration step (10 min at 110 °C), we spin-coated the Microposit S1818 positive photoresist at 4000 rpm for 60 s, and annealed at 110 °C for 1 min. Metallic contacts were patterned through direct laser lithography by using the ML3 Microwriter (from Durham Magneto Optics) and the photoresist was developed with Microposit MF-319 developer. Then, we deposited 10 nm of chromium and 25 nm of gold via thermal evaporation, and samples were immersed in acetone for 4 h for photoresist lift-off.

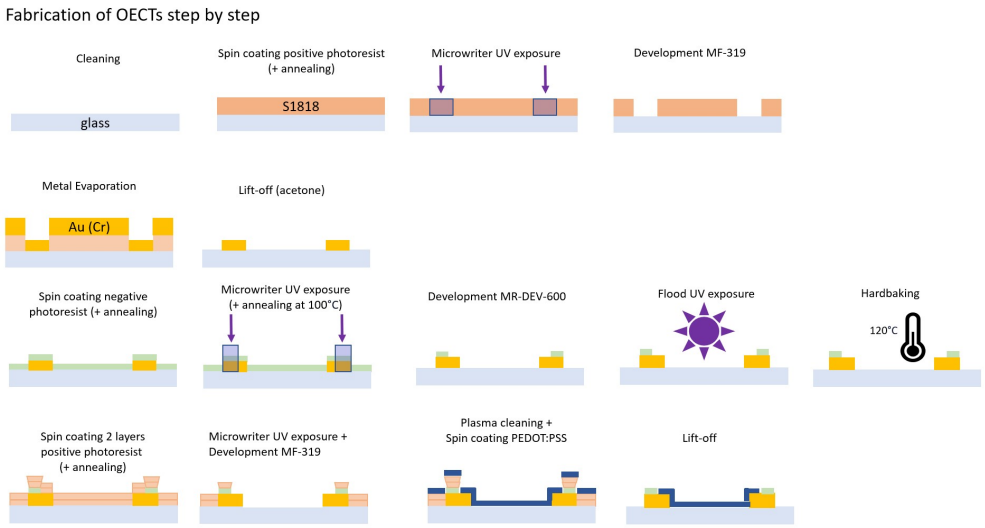

Figure 2.2: *Step by step fabrication scheme of an OECT*

Encapsulation

This procedure is aimed at insulating the conductive tracks. We spin-coated mr-DWL 5 negative photoresist (from Micro Resist Technology) at 3000 rpm for 30 s. After laser exposure, samples were baked at 100 °C for 2 min and relaxed for 1 h at room temperature. Eventually, we developed with mr-Dev 600 developer (Micro Resist Technology), and the resist was finally baked at 120 °C for 30 min.

Deposition of PEDOT:PSS

We employed the following composition for the polymeric solution:

- 94% Clevios PH1000 (Heraeus) stable water dispersion;
- 5% Ethylene glycol (EG) (Sigma Aldrich), in order to improve conductivity;
- 1% (3-glycidyloxypropyl)trimethoxysilane (GOPS) (Sigma Aldrich), a surfactant which improves adhesion onto the glass substrate by reducing surface tension;
- 0.25% P-Dodecylbenzenesulfonic acid (DBSA) (Sigma Aldrich), which promotes bonds among polymeric chains increasing the resistance against delamination;

In order to deposit the solution of PEDOT:PSS, a double layer of S1818 was spin coated and treated for 6 min in chlorobenzene for the photolithography of the channel. After the development, substrates were treated with air plasma (15 W for 2 min) and the PEDOT:PSS solution was spin-coated at 3000 rpm for 10 s, which resulted into a film thickness of 180 ± 10 nm. Finally, we annealed the samples at 120 °C for 1 h, and S1818 was finally lifted-off after 1 h in acetone.

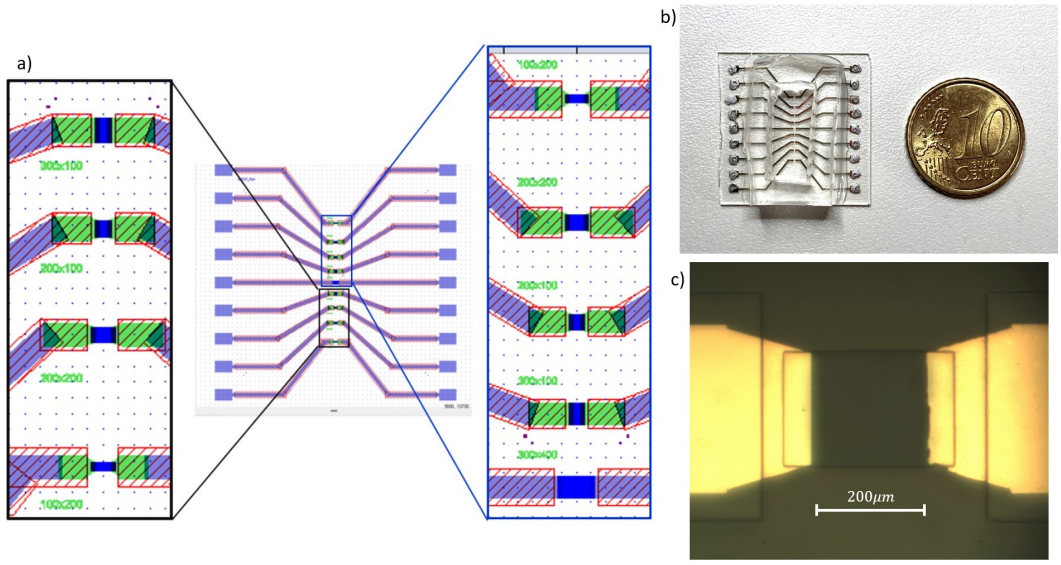

Figure 2.3: ***a)*** *The CAD scheme of the sample produced: in purple and green the conductive metal tracks, the red line delimits the negative photoresist and in blue the organic polymer. The channel dimensions are expressed in μm* ***b)*** *Picture of the sample with the PDMS well* ***c)*** *Zoom of the* $200 \times 200 (\mu m)$ *channel .*

Channel geometries

Each sample carries nine devices, with five different geometries of the channel, as shown in Tab. 2.1.

Geometry	Width, W, (μm)	Length, L, (μm)
1	100	200
2	200	200
3	200	100
4	300	100
5	300	400

Table 2.1: *Scheme of the geometries implemented in each sample*

2.2 Measurements

2.2.1 Experimental Set-up

As shown in Fig. 2.4 the experimental apparatus consists of a probe station, a Faraday cage, a Source Measurement Unit (SMU) Keysight B2912A and a MFLI Lock-in Amplifier (500 kHz; 5 MHz) (Zurich Instruments). We performed the entirety of measurements in a Faraday cage, as a precaution against external noise. The probe station

offers an optical microscope and three micromanipulators for connecting the conductive tips to the terminals of the sample.
We performed DC measurements with SMU Keysight B2912A, and AC impedance and f_{OECT} factor measurements via the MFLI Lock-in Amplifier.
The whole study was carried out with 0.1 M Phosphate buffered saline (PBS) as electrolyte, and an Ag/AgCl wire as gate electrode. Finally the electrolyte has been contained into a Polydimethylsiloxane (PDMS) well, securely attached to the glass substrate.

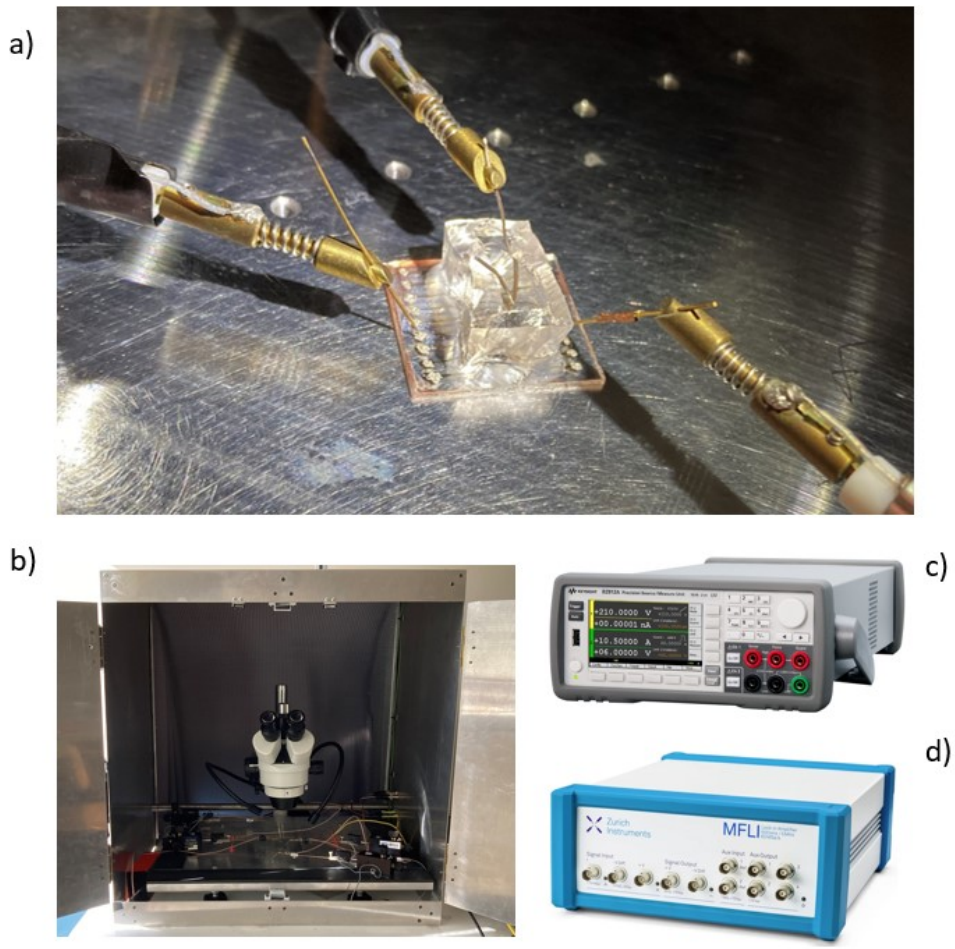

Figure 2.4: ***a)*** *OECT inside the Faraday cage, all terminals are connected via the conductive tips. The Ag/AgCl wire is dipped into the PBS electrolyte, in all measurements.* ***b)*** *Faraday cage and optical microscope.* ***c)*** *SMU Keysight B2912A* ***d)*** *Zurich MFLI Lock-in Amplifier.*

2.2.2 DC characterisation

DC measurements incude the analysis of the stationary and transient behaviour of the OECT device. In particular the stationary behaviour is investigated via Output and Transcharacteristics (transfer) curves.

Output

Output curves display the dependence of the drain current, I_D, on drain potential, V_D, at a fixed gate potential. Thus, we made the drain potential sweep in the range $-0.4\,\mathrm{V}$ to $0\,\mathrm{V}$, while keeping the gate potential constant. We repeated this proce-

dure for different gate potentials $V_G = \{0; 0.2; 0.4; 0.6; 0.8\}\, V$ in order to highlight the dependence of the drain current on the doping state of the polymer.

Transcharacteristics

Transcharacteristics show the dependence of the drain current, I_D, on the gate potential, V_G, at a fixed value of the drain potential, V_D. Therefore, we applied a constant bias to the drain and let the gate potential sweep to and fro in the range $-0.2\,\mathrm{V}$ to $0.6\,\mathrm{V}$, thus, obtaining a *forward* and a *backward* scan. We applied the same procedure at different drain potentials: namely $V_D = \{-0.4; -0.3; -0.2; -0.1\}\, V$. For each combination, we performed multiple cycles before the actual acquisition in order to activate the channel and stabilise the response of the device. Via transcharacteristic curves it is possible to obtain the profile of transconductance, g_m, at different operating regimes of the device.

Transient behaviour

Pulsed curves show the response of the drain current when a potential step is applied to the gate. We set a drain potential of $-0.3\,\mathrm{V}$ and we supplied a square wave to the gate with amplitude $V_G = 0.4\,\mathrm{V}$ and period $T = 2\,\mathrm{s}$. This measurement is aimed at testing the transient response of the device, emphasising the RC-like behaviour of the ionic circuit.

2.3 EIS

Electrochemical impedance spectroscopy (EIS) technique allows to study the impedance of the electrolyte-electrode interface as a function of frequency. Indeed, the application of a small amplitude frequency modulation to the gate electrode ideally does not alter the electrochemical potential of the interface, but it induces a detectable AC current. The frequency of the modulation is let sweep in a range, and the AC current is detected to obtain a current spectrum.
We can use the Ag/AgCl wire as reference electrode since the redox reactions between the Ag/AgCl and the electrolyte occur at a fast rate, which allows to neglect the potential drop at the gate-electrolyte interface.
We performed EIS in two different configurations:

Microelectrode configuration We implemented the microelectrode configuration by short-circuiting the drain and the source electrode and applying a AC gate potential $V_{G,AC} = 50\,\mathrm{mV}$, with no DC off-set. The measurement of the AC current at the source electrode is aimed at studying the channel-electrolyte interface, verifying the RC-like behaviour in AC conditions. By fitting the impedance spectrum, we were able to quantitatively evaluate the capacity of the channel, C_{CH}.

OECT configuration In the OECT configuration we adjusted the previous configuration by applying a bias potential to the drain, $V_D = -0.3\,\mathrm{V}$, and a DC off-set to the gate, $V_{G,DC} = 0.2\,\mathrm{V}$. From the AC source current spectrum, we were able to evaluate the bandwidth of the device.

2.4 Measurement of the f_{OECT} factor

As mentioned in Sec. 1.2.5, the dependence of the f_{OECT} on geometrical features and the operational frequency of the device is not completely understood. Adopting the logic of Eq. 1.22, the following set of equations can be written:

$$I_S = I_{ch} + f_{OECT} * I_G \tag{2.1a}$$
$$I_D = I_{ch} + (1 - f_{OECT}) * I_G \tag{2.1b}$$

where all currents are AC amplitudes. Combining the two equations, we obtain the following expressions:

$$f = \frac{I_S - I_D + I_G}{2I_G} \tag{2.2a}$$
$$I_{ch} = \frac{I_S + I_D - I_G}{2} \tag{2.2b}$$

In order to extract f_{OECT} and the channel current, I_{ch}, the current at the source, I_S, at the drain , I_D, and the gate electrode, I_G, must be known. To this end, we designed a novel apparatus to simultaneously measure the couple of AC currents at the terminal of the device for each of Eq.s 2.1a and 2.1b.

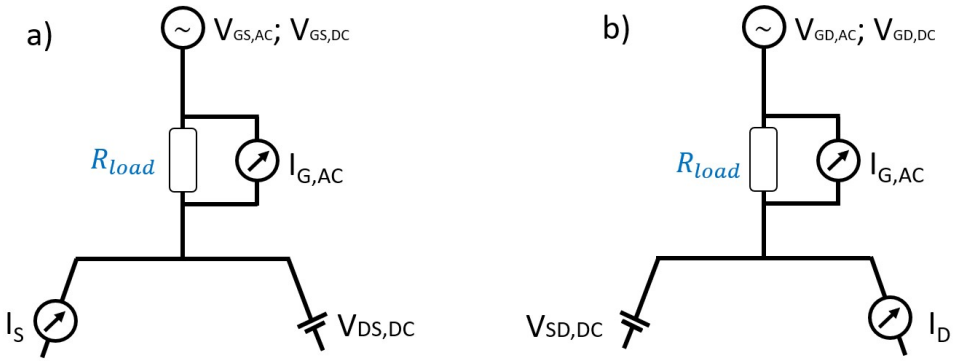

Figure 2.5: ***a)*** *Source configuration. This arrangement allows for the acquisition of the source AC current, I_S, and the gate AC current, I_G.* ***b)*** *Drain configuration. This arrangement allows for the acquisition of the drain AC current, I_D, and the gate AC current, I_G.*

In particular, for Eq. 2.1a, we implemented the scheme of Fig. 2.5 a), which we may call *Source configuration*. For Eq. 2.1b, we implemented the scheme of Fig. 2.5 b), which we may call *Drain configuration*. The basic set-up is completely equivalent to the configuration to measure the bandwith of an OECT. In the *Source configuration* a bias DC potential is applied to the drain, $V_{D,DC}$, while in the *Drain configuration* the DC potential is applied to the source $V_{S,DC}$. At the gate terminal, we supplied an AC potential, $V_{G,AC} = 50\,\text{mV}$, and a DC off-set $V_{G,DC}$. In addition, we placed a load resistance $R_{load} = 10\,\text{k}\Omega$ in series between the Ag/AgCl gate and the AC-DC supply of the lock-in. The Zurich MFLI Lock-in Amplifier allows to simultaneously acquire a current (either I_S or I_D) and a differential voltage, V_{diff}. Since the load resistor is in series with the electrolyte, the ionic gate current, I_G, can be obtained from the relation $I_{G,AC} = V_{diff,AC}/R_{load}$. Therefore, in *Source configuration* we measured I_S and I_G, while in *Drain configuration* we measured I_D and I_G. The bias DC conditions for each

configuration must be completely equivalent, hence we used the following relations to switch from the *Source* to the *Drain configuration*

$$V_{SD} = -V_{DS} \quad and \quad V_{GD} = V_{GS} - V_{DS} \tag{2.3}$$

Combining the currents for each configuration as stated by Eq.s 2.2a and 2.2b, we obtained a spectrum of f_{OECT} and I_{ch} for different channel geometries and DC potentials.

Chapter 3

Results

3.1 OECT's characterisation and comparison

3.1.1 DC characterisation

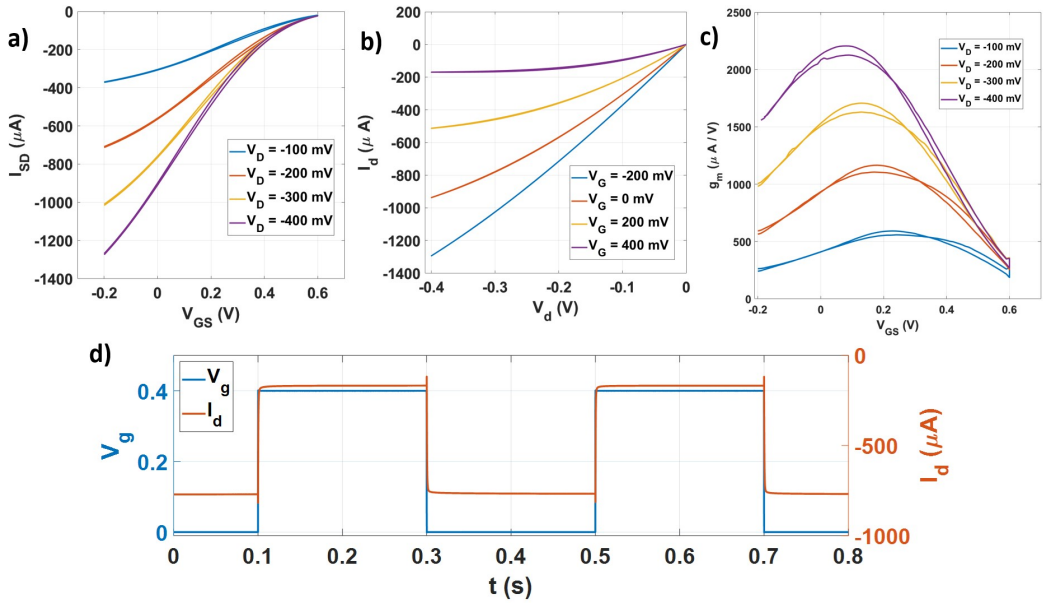

Figure 3.1: ***OECT characteristics***
a) *Transcharacteristic curves: we let V_G sweep in the range $-0.2\,\mathrm{V}$ to $0.6\,\mathrm{V}$, while keeping V_D constant. We repeated the same procedure for $V_D = \{-0.4; -0.3; -0.2; -0.1\}\,V$* ***b)*** *Output curves: we let V_D sweep in the range $-0.4\,\mathrm{V}$ to $0\,\mathrm{V}$, while keeping V_D constant. We repeated the same procedure for $V_G = \{-0.2; 0; 0.2; 0.4\}\,V$* ***c)*** *Transconductance, g_m, was extracted from transcharacteristic curves plotted in panel* ***a)****.* ***d)*** *Transient behaviour: we applied a constant drain voltage $V_D = -0.3\,\mathrm{V}$ and we applied a square wave at the gate with amplitude $V_G = 0.4\,\mathrm{V}$ and period $T = 0.4\,\mathrm{s}$.*
The device studied has the following geometry: the channel has a surface of $W \times L = 300 \times 100\,\mu\mathrm{m}^2$, and a thickness of $T = (180 \pm 10)\,\mathrm{nm}$.

The device studied has a ratio of $\frac{W}{L} = 3$ and a thickness of $T = (180 \pm 10)\,\mathrm{nm}$. OECT Transcharacteristics are reported in Fig. 3.1 a), and show how the applied gate voltage effectively modulates the electronic current flowing in the channel. As expected from Eq. 1.15, I_{SD} goes to zero as $V_G = V_t$, where V_t is the threshold voltage. For each set of gate and drain potentials the *forward* and the *backward* scan do not overlap completely: in the *forward* scan, currents are slightly larger than in the *backward* scan.

This is due to the finite ion mobility of the electrolyte: in the *backward* scan, V_G is decreasing, reducing the de-doping of the channel. However, when the measurement is performed, the ionic concentration may still be higher than the stationary one, which results into a lower current. Fig. 3.1 c) displays the dependence of transconductance, g_m, on V_G. The maximum of g_m corresponds to the peak of the amplification of the device, and its position runs towards lower V_G values as V_D becomes more negative. The output curves are plotted in Fig. 3.1 b). The device behaves consistently with the model implemented in Sec. 1.2.3. When no bias potential is applied to the drain, the drain current is zero, and, as V_G increases, $|I_D|$ decreases accordingly as a result of the ongoing de-doping of the channel. The transient behaviour of Fig. 3.1 c) matches the RC transient response of the model of Sec. 1.2.4. The presence of a spike at the beginning of each transient can be associated to the condition $\tau_i \leq f_{OECT} * \tau_e$, where $\tau_e \quad and \quad \tau_i$ are the electronic and ionic time constants respectively.

3.1.2 Mobility extraction

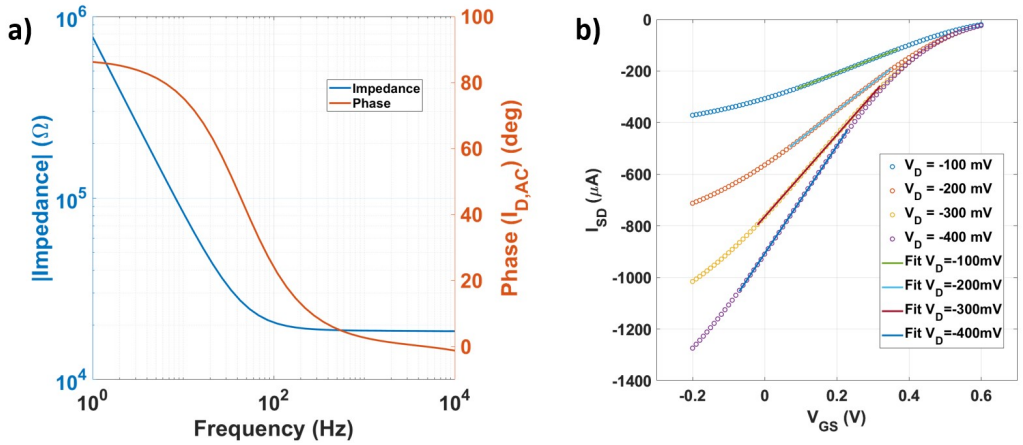

Figure 3.2: ***EIS and mobility extraction***
a) *Bode Plot of EIS measurement* ***b)*** *Fit of the Transfer curves in the linear region of the device in order to extract the hole mobility, μ_p, and the threshold potential, V_t.*

Fig. 3.2 a) shows the EIS performed in the Microelectrode configuration. The dependence of impedance and phase on the frequency is consistent with an RC series: impedance decreases at high frequencies, while phase is in quadrature at low-frequencies. Performing the fit of the impedance profile using the RC series model, we were able to extract the capacitance of the channel: $C_{ch} = (192 \pm 10)\,\mathrm{nF}$.

By fitting transfer curves in Fig. 3.1 a) in the linear region, we were able to estimate hole mobility, μ_p. In the homic region the source current can be written as

$$I_{SD} = \mu_p C^* \frac{WT}{L} V_{DS} * [V_t - V_{GS}] \tag{3.1}$$

with the same meaning of symbols of Sec. 1.2.3, and namely $C^* = C_{ch}/WLT$. In our device volumetric capacity is $C^* = (36 \pm 4)\,\mathrm{nF\,m^{-3}}$, which is consistent with literature findings [31]. Performing a linear fit in the form

$$I_S = A * V_{GS} + B \tag{3.2}$$

it follows that

$$\mu_p = \frac{L}{C^*WT|V_{DS}|} * A \quad and \quad V_t = -\frac{B}{A} \tag{3.3}$$

We performed the fits on *forward* scans only and results are summarised in Tab. 3.1. Mobilities are consistent with those in literature for this type of devices [24].

V_D (mV)	-100	-200	-300	-400
μ_p ($\mathrm{cm^2\,V^{-1}\,s^{-1}}$)	2.846 ± 0.001	2.815 ± 0.002	2.747 ± 0.003	2.711 ± 0.003
V_t (V)	0.5804 ± 0.0001	0.5274 ± 0.0003	0.7073 ± 0.0005	0.4359 ± 0.0005

Table 3.1: *Hole mobility, μ_p, and threshold potential, V_t, extracted at different drain potentials. Errors were obtained by means of error propagation.*

3.1.3 AC characterisation

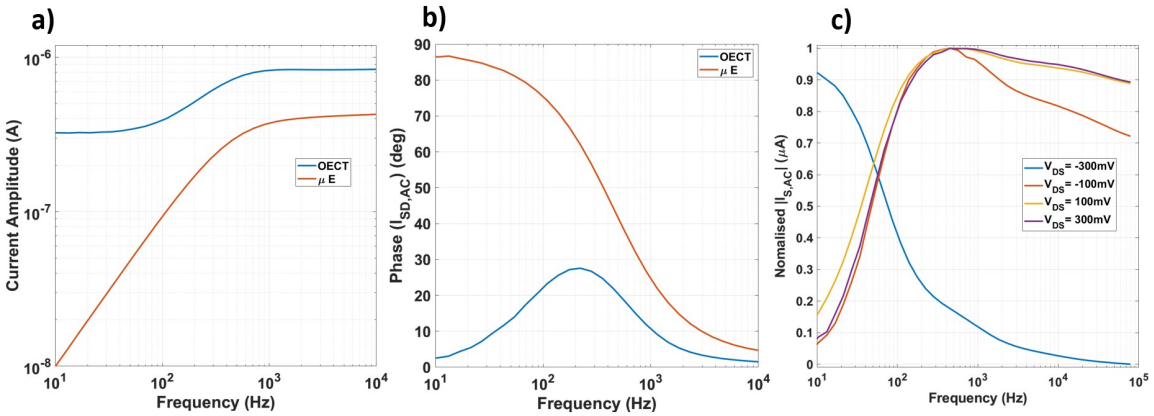

Figure 3.3: ***AC characterisation***
a) *Current spectrum of a microelectrode and of an OECT* ***b)*** *Phase spectrum of a microelectrode and an OECT* ***c)*** *normalised source AC current*

Fig. 3.3 displays the comparison between a microelectrode and an OECT when the same $V_G = 0.2\,\mathrm{V}$ is applied. In panel a) of Fig. 3.3, the behaviour of the current spectrum is displayed: the amplification property of the OECT is manifest at low frequencies, where the device shows low-pass filter characteristics with respect to the microelectrode. In panel b), the phase of the microelectrode is consistent with the one of an RC circuit, while the OECT's phase exhibits a more complex trend. Fig. 3.3 c) shows the spectrum of the normalised g_m, highlighting how the transistor effect emerges at lower frequencies. Indeed, the amplification is tightly linked to the ionic charge stored in the polymeric channel, which is modelled as a capacitor. Because of the finite mobility of ions in the bulk of the polymer, at high-frequency regimes only a small amount of ions is stored in the channel, which results into limited amplification properties. Conversely, at low-frequency regimes, ions can permeate the polymeric bulk in higher quantities, giving rise to the transistor effect.

3.2 f_{OECT}

3.2.1 Determination of f_{OECT}

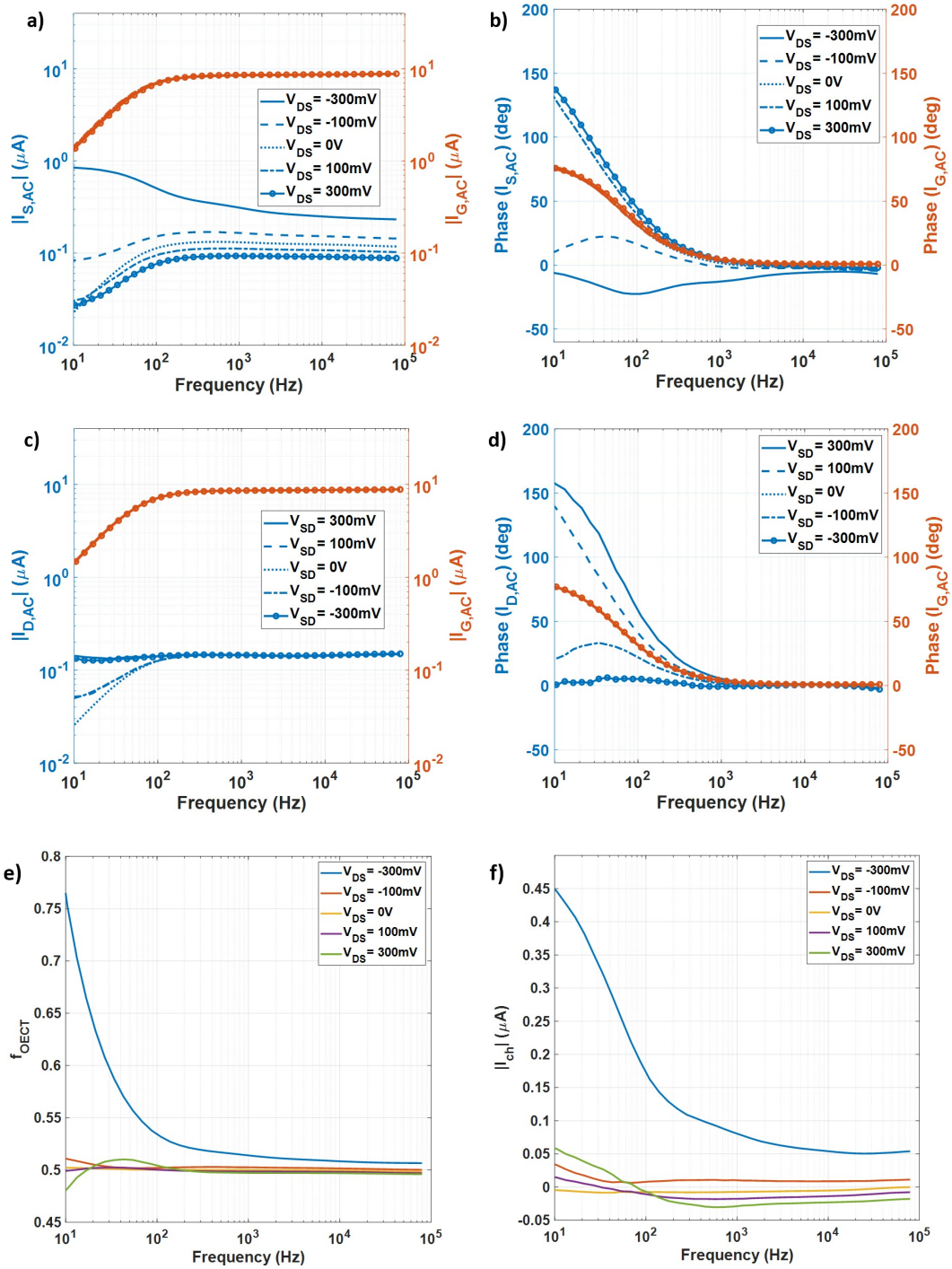

Figure 3.4: ***Determination of*** f_{OECT} ***factor***
a) *Source and gate AC currents acquired in Source configuration* ***b)*** *Phase of the source and gate AC currents acquired in Source configuration* ***c)*** *Drain and gate AC currents acquired in Source configuration* ***d)*** *Phase of drain and of gate AC currents acquired in Source configuration* ***e)*** f_{OECT} *spectrum* ***f)*** *Channel current,* I_{ch}*, spectrum.*
In all measurements $V_{GS} = 0.2\,\mathrm{V}$*.*

The current and phase measurements of the *Source* and *Drain* configurations introduced in Sec. 2.4 are reported in Fig. 3.4 a) to d). We set the gate potential at $V_G =$

0.2 V and applied five different drain potentials $V_{DS} = \{-0.3; -0.1; 0; +0.1; +0.3\}$ V. We made the frequency of the AC perturbation sweep in the range $[10; 10^5]$ Hz. The gate current displays a capacitive behaviour at low frequencies, where its phase goes in quadrature. Inspecting Fig. 3.4 a) and c) more in detail, the source current and the drain current at $V_{DS} = 0 = V_{SD}$ report a systematic offset. In this configuration the channel is completely symmetric, and the current measured at one terminal should be half the gate current. However, $I_{S,AC}$ and $I_{D,AC}$ are smaller than $I_{G,AC}$ of about a factor ten. This is probably caused by the poor adhesion of the encapsulation layer. The delamination of the negative photoresist from the electrical feedlines produces a parasitic AC current caused by the capacitive coupling of the gold electrodes with the surrounding electrolyte. Such effect is supported by Fig. 3.4 a), where we observe an increase in the AC gate current amplitude and a shift of the RC low-pass cutoff towards smaller frequencies. This effect cancels out in the f_{OECT}, while it is predominant in the channel current I_{ch}. Therefore, we estimated the offset as the difference between the half of the gate current and the current at the source or drain terminal, and added the correction in the determination of I_{ch}. By means of Eq.s 2.2, we obtained curves shown in Fig. 3.4 e) and f).

3.2.2 Comparison of f_{OECT}

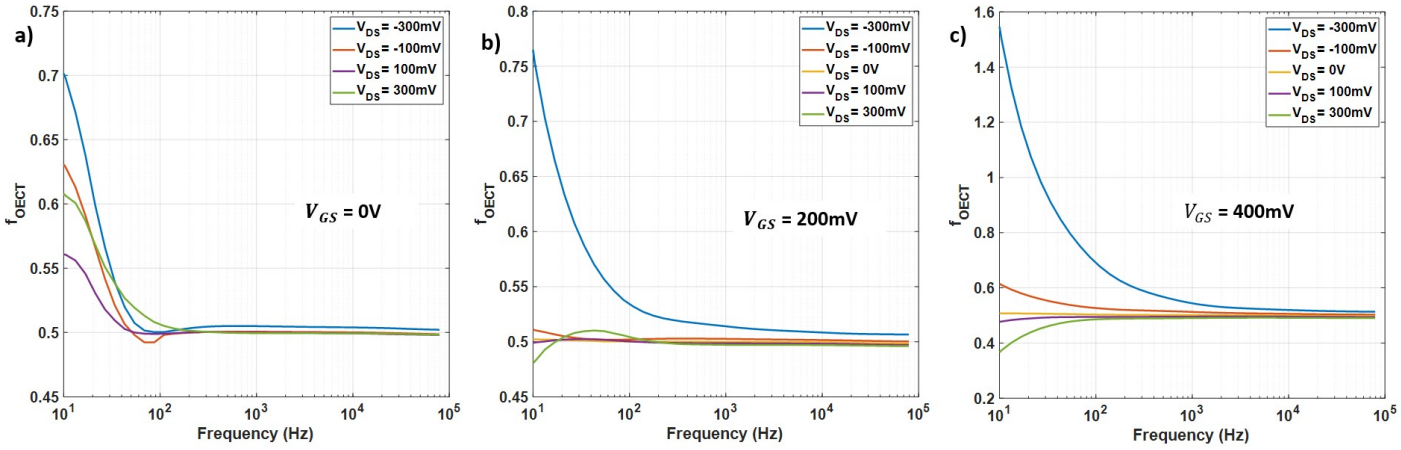

Figure 3.5: f_{OECT} ***factor results***
a) *f_{OECT} factor spectrum at $V_{GS} = 0$ V* ***b)*** *f_{OECT} factor spectrum at $V_{GS} = 0.2$ V* ***c)*** *f_{OECT} factor spectrum at $V_{GS} = 0.4$ V*

Fig. 3.5 shows the results of the f_{OECT} extracted with the procedure of Sec. 3.2.1 for different gate potentials $V_G = \{0; 0.2; 0.4; \}$ V. In the high frequency regime $f_{OECT} \to \frac{1}{2}$, while at low frequencies, it displays a more complex behaviour depending on the set of gate and drain DC potentials applied. First, for negative V_{DS}, f_{OECT} is directly correlated to V_{GS}, as shown in Fig. 3.5 b) and c). For positive drain potentials, f_{OECT} decreases as V_{GS} increases. When $V_{DS} = 0$ V, $f_{OECT} \approx \frac{1}{2}$ through the whole spectrum. The comparison of the curves for the same V_{GS} highlights how configurations with opposite V_{DS} show opposite trends, which is expected given the symmetry of the device. In the configuration $V_{GS} = 0.4$ V and $V_{DS} = -0.3$ V, f_{OECT} exceeds 1: this may be due to the poor insulation of the gold electrodes. The configuration at $V_{GS} = 0$ V confirms the above observations for $V_{DS} = -0.3$ V, while it exhibits some peculiar features at the other drain potentials. The complementarity of configurations with

opposite drain potential is lost and, for $V_{DS} = -0.1\,\mathrm{V}$, f_{OECT} is significantly larger than the equivalent at $V_{GS} = 0.2\,\mathrm{V}$.

Still, these results can be explained taking into consideration the de-doping process of the channel and its dependence on frequency. In the high frequency regime, the current passing through the PEDOT:PSS-electrolyte interface is displacement current and no charge accumulation occurs. The transistor effect is highly suppressed and the OECT tends to behave as a microelectrode. In a microelectrode, source and drain are completely symmetric, which entails $f_{OECT} = \frac{1}{2}$.

In the low-frequency regime, charge accumulation is significant. When no bias DC potential is applied to the drain, $V_{DS} = 0$, since $V_{GS} = V_{GD}$, de-doping occurs uniformly along the channel and the OECT should be completely symmetric, yielding again a $f_{OECT} = \frac{1}{2}$, as observed in Fig. 3.5 b) and c). In addition, this suggests inspecting the f_{OECT} for the configuration $V_{GS} = 0\,\mathrm{V}$, $V_{DS} = 0\,\mathrm{V}$: the anomalies of the configuration $V_{GS} = 0\,\mathrm{V}$ could be better understood if f_{OECT} showed a dependence on frequency when no DC potentials are applied, which would be a parameter of the intrinsic asymmetry of the channel.

When a potential is applied to the drain, $V_{GS} \neq V_{GD}$, and de-doping occurs differently at the two terminals as a consequence of asymmetric cation accumulation along the channel. Namely, if $V_{DS} < 0$, the concentration of cations increases more in the drain terminal than at the source terminal, which results into the drain terminal to be more de-doped than the source. Therefore, conductivity is lower in the region of the drain, which results into $f_{OECT} > \frac{1}{2}$. Conversely, if $V_{DS} > 0$, the drain terminal is de-doped less than the source and $f_{OECT} < \frac{1}{2}$. This trend is highlighted by the curves in Fig. 3.5 b) and c), but not by those in panel a), which may need further analysis as described above.

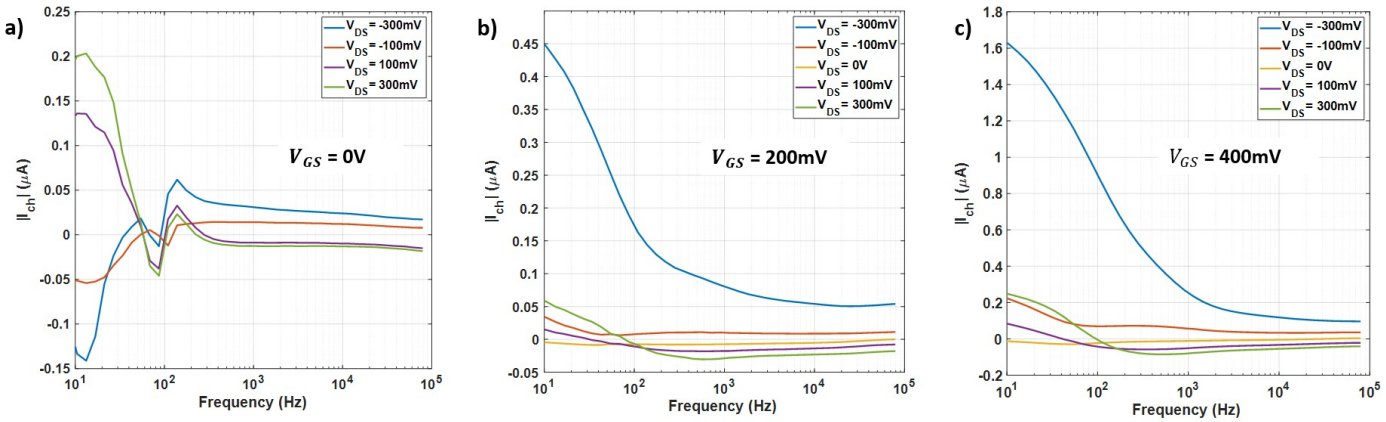

Figure 3.6: ***Channel current results***
a) *Channel current spectrum at* $V_{GS} = 0\,\mathrm{V}$ ***b)*** *Channel current spectrum at* $V_{GS} = 0.2\,\mathrm{V}$ ***c)*** *Channel current spectrum at* $V_{GS} = 0.4\,\mathrm{V}$

Fig. 3.6 shows how the channel AC current tends to a constant value at high frequencies, while it increases at lower frequencies, which is consistent with the dependence of ion transport on frequency introduced in the previous paragraph. Configuration at $V_{DS} = -0.3\,\mathrm{V}$ clearly follows this trend, while other currents show a milder increase in the lower bound of the spectrum. The negative values assumed by the channel currents came as an unexpected result. This might be the consequence of the systematic error mentioned in Sec. 3.2.1 induced by the non-ideality of the device. However, the configuration at $V_{GS} = 0\,\mathrm{V}$ displays some anomalous instability for all drain potentials applied. This suggests that channel currents need further research in order to discern

between an anomalous behaviour or the presence of a process which has not been taken into account in the model of ion transport developed for f_{OECT}.

Conclusions

PEDOT:PSS-based OECTs are proving to be a versatile alternative to traditional inorganic based devices in numerous fields of biological and medical research thanks to both high transconductances and low-cost fabrication. In order to fully exploit their potential, it is necessary to study extensively the dependence of the response on constructive parameters and the working point of the device. For OECTs employed as impedance sensors, sensitivity is found to be dependent on f_{OECT} factor: a parameter accounting for the fraction of ionic gate current which contributes to the source current. The behaviour of this parameter on the operating frequency and the DC potentials applied to the terminals has not been completely understood, yet. In this research, we investigated this question for an OECT with a width-length ratio of $\frac{W}{L} = 3$, showing a hole mobility of $\mu \approx (2.78 \pm 0.07)\,\mathrm{cm^2\,V^{-1}\,s^{-1}}$, which is consistent with results in literature, and a threshold potential of $V_t \approx (0.56 \pm 0.14)\,\mathrm{V}$. The volumetric capacitance of the device is $C^* = (36 \pm 4)\,\mathrm{F\,cm^{-3}}$, which is consistent with literature findings as well.

From the spectra of f_{OECT} in the range of frequencies $f = [10; 10^5]\,\mathrm{Hz}$, we found out that $f_{OECT} \to \frac{1}{2}$, for $f > 10\,\mathrm{kHz}$: in the high-frequency regime, charge transport in the PEDOT:PSS layer is only determined by the ionic capacitive displacement current at the PEDOT:PSS-electrolyte interface.

In the low-frequency regime, when a non zero potential is applied to the gate, f_{OECT} is a non trivial function of the bias DC potentials applied to the gate and to the drain terminals. Indeed, in this condition, despite the limited ionic mobility, cations accumulate in the channel according to the potentials applied. This leads to a non uniform distribution of cations, which affects the local doping state of the polymer, and, hence, conductivity. In particular, higher concentration of cations results into lower doping state and lower conductivity.

For $V_{DS} < 0\,\mathrm{V}$, we found that $f_{OECT} > \frac{1}{2}$ and shows a positive correlation with the gate potential applied. The concentration of cations in the drain region is higher than in the source, therefore the current at the drain is smaller than at the source. Conversely, for $V_{DS} > 0\,\mathrm{V}$, because of the higher concentration of cations at the source terminal, $f_{OECT} < \frac{1}{2}$ and displays a negative correlation with the gate potential.

In our analysis we were able to extract the channel current,I_{ch} , as well. The current in the channel tends to constant values at high frequencies, and it increases in the low frequency regime, which is consistent with the dynamics of ionic transport introduced above. Indeed, larger f_{OECT} factors are measured at lower frequencies when the source (or drain) electrodes are depleted from cations, which entails a larger local doping level for PEDOT:PSS and therefore higher electronic currents.

Despite our main findings, this experiment was affected by some non-idealities caused by parasitic currents arising from the leaky encapsulation of devices. Since f_{OECT} factor depends on the difference of the source and drain current, its extraction was not affected by this systematic error. On the other hand, such effects led to an underestimation of the channel current, which is a function of the sum of the source and the drain currents. This had a detrimental impact on the configuration

at $V_{GS} = 0\,\mathrm{V}$, where the channel currents show an anomalous instability towards the lower frequencies. Consequently, additional examination is needed to distinguish whether the device exhibits non-ideality or if there is a novel undiscovered process that has not yet been considered.

Bibliography

[1] Magnus Berggren and Agneta Richter-Dahlfors. "Organic Bioelectronics". In: *Advanced Materials* 19 (Oct. 2007), pp. 3201–3213. DOI: 10.1002/adma.200700419.

[2] Jonathan Rivnay, Róisín M. Owens, and George G. Malliaras. "The Rise of Organic Bioelectronics". In: *Chem. Mater.* 26.1 (Jan. 2014). Publisher: American Chemical Society, pp. 679–685. ISSN: 0897-4756. DOI: 10.1021/cm4022003. URL: https://doi.org/10.1021/cm4022003 (visited on 05/03/2023).

[3] Bryan E. Kohler and I. D. W. Samuel. "Experimental determination of conjugation lengths in long polyene chains". en. In: *The Journal of Chemical Physics* 103.14 (Oct. 1995), pp. 6248–6252. ISSN: 0021-9606, 1089-7690. DOI: 10.1063/1.470402. URL: https://pubs.aip.org/aip/jcp/article/103/14/6248-6252/481479 (visited on 05/03/2023).

[4] Alan J. Heeger. "Semiconducting and Metallic Polymers: The Fourth Generation of Polymeric Materials". In: *J. Phys. Chem. B* 105.36 (Sept. 2001). Publisher: American Chemical Society, pp. 8475–8491. ISSN: 1520-6106. DOI: 10.1021/jp011611w. URL: https://doi.org/10.1021/jp011611w (visited on 05/03/2023).

[5] Mahiar Hamedi, Robert Forchheimer, and Olle Inganäs. "Towards woven logic from organic electronic fibres". en. In: *Nature Mater* 6.5 (May 2007). Number: 5 Publisher: Nature Publishing Group, pp. 357–362. ISSN: 1476-4660. DOI: 10.1038/nmat1884. URL: https://www.nature.com/articles/nmat1884 (visited on 05/03/2023).

[6] Maria Daniela Angione et al. "Interfacial electronic effects in functional biolayers integrated into organic field-effect transistors". In: *Proc Natl Acad Sci U S A* 109.17 (Apr. 2012), pp. 6429–6434. ISSN: 0027-8424. DOI: 10.1073/pnas.1200549109. URL: https://www.ncbi.nlm.nih.gov/pmc/articles/PMC3340085/ (visited on 05/03/2023).

[7] Dion Khodagholy et al. "In vivo recordings of brain activity using organic transistors". eng. In: *Nat Commun* 4 (2013), p. 1575. ISSN: 2041-1723. DOI: 10.1038/ncomms2573.

[8] Roger Mortimer, Aubrey Dyer, and John Reynolds. "Electrochromic organic and polymeric materials for display applications". In: *Displays* 27 (Jan. 2006), pp. 2–18. DOI: 10.1016/j.displa.2005.03.003.

[9] Elisabeth Smela. "Conjugated Polymer Actuators". en. In: *MRS Bulletin* 33.3 (Mar. 2008). Publisher: Cambridge University Press, pp. 197–204. ISSN: 1938-1425, 0883-7694. DOI: 10.1557/mrs2008.45. URL: https://www.cambridge.org/core/journals/mrs-bulletin/article/abs/conjugated-polymer-actuators/74ACEEF0C40DB610F6EC7E9B61C98E8E (visited on 05/03/2023).

[10] Sarah M. Richardson-Burns, Jeffrey L. Hendricks, and David C. Martin. "Electrochemical polymerization of conducting polymers in living neural tissue". eng. In: *J Neural Eng* 4.2 (June 2007), pp. L6–L13. ISSN: 1741-2560. DOI: 10.1088/1741-2560/4/2/L02.

[11] K. Norrman, A. Ghanbari-Siahkali, and N. B. Larsen. "6 Studies of spin-coated polymer films". en. In: *Annu. Rep. Prog. Chem., Sect. C: Phys. Chem.* 101.0 (Oct. 2005). Publisher: The Royal Society of Chemistry, pp. 174–201. ISSN: 1460-4787. DOI: 10.1039/B408857N. URL: https://pubs.rsc.org/en/content/articlelanding/2005/pc/b408857n (visited on 05/08/2023).

[12] P. Cooreman et al. "Impedimetric immunosensors based on the conjugated polymer PPV". eng. In: *Biosens Bioelectron* 20.10 (Apr. 2005), pp. 2151–2156. ISSN: 0956-5663. DOI: 10.1016/j.bios.2004.08.029.

[13] Peter Asberg and Olle Inganäs. "Hydrogels of a conducting conjugated polymer as 3-D enzyme electrode". eng. In: *Biosens Bioelectron* 19.3 (Nov. 2003), pp. 199–207. ISSN: 0956-5663. DOI: 10.1016/s0956-5663(03)00220-3.

[14] Laura Basiricò et al. "Inkjet printing of transparent, flexible, organic transistors". en. In: *Thin Solid Films* 520.4 (Dec. 2011), pp. 1291–1294. ISSN: 00406090. DOI: 10.1016/j.tsf.2011.04.188. URL: https://linkinghub.elsevier.com/retrieve/pii/S0040609011010297 (visited on 05/06/2023).

[15] Francesco Decataldo et al. "Fast and real-time electrical transistor assay for quantifying SARS-CoV-2 neutralizing antibodies". en. In: *Commun Mater* 3.1 (Jan. 2022). Number: 1 Publisher: Nature Publishing Group, pp. 1–9. ISSN: 2662-4443. DOI: 10.1038/s43246-022-00226-6. URL: https://www.nature.com/articles/s43246-022-00226-6 (visited on 05/06/2023).

[16] Francesco Decataldo et al. "Organic Electrochemical Transistors as Versatile Tool for Real-Time and Automatized Viral Cytopathic Effect Evaluation". en. In: *Viruses* 14.6 (June 2022). Number: 6 Publisher: Multidisciplinary Digital Publishing Institute, p. 1155. ISSN: 1999-4915. DOI: 10.3390/v14061155. URL: https://www.mdpi.com/1999-4915/14/6/1155 (visited on 05/06/2023).

[17] J. Y. Wong, R. Langer, and D. E. Ingber. "Electrically conducting polymers can noninvasively control the shape and growth of mammalian cells". eng. In: *Proc Natl Acad Sci U S A* 91.8 (Apr. 1994), pp. 3201–3204. ISSN: 0027-8424. DOI: 10.1073/pnas.91.8.3201.

[18] Alwin M. D. Wan et al. "Electrical control of cell density gradients on a conducting polymer surface". en. In: *Chem. Commun.* 35 (Aug. 2009). Publisher: The Royal Society of Chemistry, pp. 5278–5280. ISSN: 1364-548X. DOI: 10.1039/B911130A. URL: https://pubs.rsc.org/en/content/articlelanding/2009/cc/b911130a (visited on 05/06/2023).

[19] Joakim Isaksson et al. "Electronic control of Ca2+ signalling in neuronal cells using an organic electronic ion pump". eng. In: *Nat Mater* 6.9 (Sept. 2007), pp. 673–679. ISSN: 1476-1122. DOI: 10.1038/nmat1963.

[20] H. S. White, G. P. Kittlesen, and M. S. Wrighton. *Chemical derivatization of an array of three gold microelectrodes with polypyrrole: Fabrication of a molecule-based transistor*. Tech. rep. Publication Title: Massachusetts Inst. of Tech. Report ADS Bibcode: 1984mit..reptS....W. Sept. 1984. URL: https://ui.adsabs.harvard.edu/abs/1984mit..reptS....W (visited on 05/06/2023).

[21] Jonathan Rivnay et al. “Organic electrochemical transistors”. en. In: *Nat Rev Mater* 3.2 (Jan. 2018). Number: 2 Publisher: Nature Publishing Group, pp. 1–14. ISSN: 2058-8437. DOI: 10.1038/natrevmats.2017.86. URL: https://www.nature.com/articles/natrevmats201786 (visited on 05/06/2023).

[22] Maria Nikolou and George G. Malliaras. “Applications of poly(3,4-ethylenedioxythiophene) doped with poly(styrene sulfonic acid) transistors in chemical and biological sensors”. en. In: *The Chemical Record* 8.1 (2008), pp. 13–22. ISSN: 1528-0691. DOI: 10.1002/tcr.20133. URL: https://onlinelibrary.wiley.com/doi/abs/10.1002/tcr.20133 (visited on 05/08/2023).

[23] D. A. Bernards and G. G. Malliaras. “Steady-State and Transient Behavior of Organic Electrochemical Transistors”. en. In: *Advanced Functional Materials* 17.17 (2007). _eprint: https://onlinelibrary.wiley.com/doi/pdf/10.1002/adfm.200601239, pp. 3538–3544. ISSN: 1616-3028. DOI: 10.1002/adfm.200601239. URL: https://onlinelibrary.wiley.com/doi/abs/10.1002/adfm.200601239 (visited on 05/06/2023).

[24] Jacob T. Friedlein, Robert R. McLeod, and Jonathan Rivnay. “Device physics of organic electrochemical transistors”. en. In: *Organic Electronics* 63 (Dec. 2018), pp. 398–414. ISSN: 1566-1199. DOI: 10.1016/j.orgel.2018.09.010. URL: https://www.sciencedirect.com/science/article/pii/S1566119918304683 (visited on 05/12/2023).

[25] L. A. Lasky et al. “An endothelial ligand for L-selectin is a novel mucin-like molecule”. eng. In: *Cell* 69.6 (June 1992), pp. 927–938. ISSN: 0092-8674. DOI: 10.1016/0092-8674(92)90612-g.

[26] Takatsugu Okegawa et al. “The role of cell adhesion molecule in cancer progression and its application in cancer therapy”. eng. In: *Acta Biochim Pol* 51.2 (2004), pp. 445–457. ISSN: 0001-527X.

[27] H. Perinpanayagam et al. “Early cell adhesion events differ between osteoporotic and non-osteoporotic osteoblasts”. eng. In: *J Orthop Res* 19.6 (Nov. 2001), pp. 993–1000. ISSN: 0736-0266. DOI: 10.1016/S0736-0266(01)00045-6.

[28] Scott I. Simon and Chad E. Green. “Molecular mechanics and dynamics of leukocyte recruitment during inflammation”. eng. In: *Annu Rev Biomed Eng* 7 (2005), pp. 151–185. ISSN: 1523-9829. DOI: 10.1146/annurev.bioeng.7.060804.100423.

[29] Zhonglan Tang et al. “Shear stress-dependent cell detachment from temperature-responsive cell culture surfaces in a microfluidic device”. en. In: *Biomaterials* 33.30 (Oct. 2012), pp. 7405–7411. ISSN: 0142-9612. DOI: 10.1016/j.biomaterials.2012.06.077. URL: https://www.sciencedirect.com/science/article/pii/S0142961212007272 (visited on 06/21/2023).

[30] Filippo Bonafè et al. “AC amplification gain in organic electrochemical transistors for impedance-based single cell sensors”. en. In: *Nat Commun* 13.1 (Sept. 2022). Number: 1 Publisher: Nature Publishing Group, p. 5423. ISSN: 2041-1723. DOI: 10.1038/s41467-022-33094-2. URL: https://www.nature.com/articles/s41467-022-33094-2 (visited on 05/12/2023).

[31] Anton V. Volkov et al. “Understanding the Capacitance of PEDOT:PSS”. en. In: *Advanced Functional Materials* 27.28 (2017), p. 1700329. ISSN: 1616-3028. DOI: 10.1002/adfm.201700329. URL: https://onlinelibrary.wiley.com/doi/abs/10.1002/adfm.201700329 (visited on 06/21/2023).